Geochronology, 6, 585–605, 2024
https://doi.org/10.5194/gchron-6-585-2024

In situ rubidium–strontium geochronology of white mica in young metamafic and metasomatic rocks from Syros: testing the limits of laser-ablation triple-quadrupole inductively coupled plasma mass spectrometer mica dating using different anchoring approaches

Jesús Muñoz-Montecinos[1], Andrea Giuliani[2,3], Senan Oesch[2], Silvia Volante[1], Bradley Peters[2], and Whitney Behr[1]

[1]Department of Earth and Planetary Sciences, Institute of Geology, ETH Zurich, Sonneggstrasse 5, 8092, Zurich, Switzerland
[2]Department of Earth and Planetary Sciences, Institute of Geochemistry and Petrology, ETH Zurich, Clausiusstrasse 25, Zurich, 8092, Switzerland
[3]Earth and Planets Laboratory, Carnegie Institution for Science, 5241 Broad Branch Rd NW, Washington, DC 20015, USA

Correspondence: Jesús Muñoz-Montecinos (jmunoz@ethz.ch)

Received: 11 June 2024 – Discussion started: 2 July 2024
Revised: 13 September 2024 – Accepted: 20 September 2024 – Published: 13 November 2024

Abstract. The recent development of laser-ablation triple-quadrupole inductively coupled plasma mass spectrometry (LA-ICP-MS/MS) has revolutionized rubidium–strontium (Rb–Sr) mica dating, allowing us to obtain isotopic data within their microstructural context. While effective for old and felsic materials, this method presents challenges for young metamafic and metasomatic rocks due to limited radiogenic ingrowth associated with low Rb/Sr and young ages. We quantitatively address these limitations by combining laser-ablation ICP-MS/MS and MC-ICP-MS data for coexisting white mica and epidote, respectively, for 10 Cenozoic metamorphic rocks from Syros (Greece). White mica analyses from metamafic and metasomatic rocks yield limited Rb/Sr spread, which typically does not exceed an order of magnitude ($^{87}Rb/^{86}Sr = 14$ to 231 for the combined dataset), and low radiogenic $^{87}Sr/^{86}Sr$ (generally < 0.8), resulting in high age uncertainties of typically 10 to 50 % relative standard error (RSE), thus hampering robust geological interpretations. Epidote $^{87}Sr/^{86}Sr$ values range between ~ 0.705 and 0.708. The former is typically expected for unaltered metamafic materials, whereas the latter is interpreted to reflect fluid–rock interaction along shear zones, with fluids derived from or having interacted with more radiogenic lithologies. These atypical values suggest that a commonly assumed value of 0.703 for mafic rocks may not always be representative. Anchoring white mica Rb–Sr to epidote $^{87}Sr/^{86}Sr$ data improves age accuracy and precision substantially (e.g., 29 ± 17 Ma vs. 47.2 ± 4.4 Ma for sample SYGR36). The new ages obtained in this study are consistent with multiple events previously recorded on Syros and the Cyclades blueschists unit including (i) metasomatism and metamorphism at near peak to epidote blueschist-facies conditions during early exhumation (ca. 47 to 41 Ma) and (ii) a late stage of high-pressure exhumation and metasomatism transitioning to blueschist and greenschist-facies conditions (ca. 21 to 20 Ma). Anchored white mica Rb–Sr ages in mafic rocks allow us to discriminate events of fluid–rock interactions and metasomatism associated with shear zone deformation at the subduction interface.

1 Introduction

Subduction zones host a wide range of mechanical and chemical processes that occur at various spatial and temporal scales, including seismicity, element transfer, volcanism, and orogenesis (e.g., Breeding et al., 2004; Burg and Bouilhol, 2019; Muñoz-Montecinos et al., 2021; Li et al., 2021; Wirth et al., 2022; Bastias et al., 2023; Rubatto et

al., 2023). These processes are temporally associated with metamorphism, fluid–rock interactions and metasomatism at depth and occur over timescales ranging from those of steady-state tectonics (e.g., nappe stacking over millions of years; Rubatto et al., 2011; Holtmann et al., 2022) to nearly instantaneous mineral growth and fluid flow (John et al., 2012; Beinlich et al., 2020). Constraining the timing of high-pressure and low-temperature (HP–LT) mineral growth and fabric development is therefore crucial for understanding deep tectono-thermal processes. However, accurately dating these subduction-related metamorphic events remains challenging.

Compared to felsic rocks, dating metamafic rocks is challenging due to the paucity of minerals amenable to geochronology. While the uranium–lead (U–Pb) system has been employed to date HP–LT mafic metamorphic rocks, it relies on the presence of U-bearing accessory phases such as zircon, allanite, titanite, rutile, and apatite, which may be scarce, too small to be targeted, or have low U concentrations (e.g., Timmermann et al., 2004; Rubatto et al., 2011; Regis et al., 2014; Engi et al., 2017; Holtmann et al., 2022; Volante et al., 2024, and references therein). Additionally, it is challenging to link microstructures with U–Pb dates of accessory minerals due to their often ambiguous textural association with the microfabrics. Therefore, alternative minerals and systematics are essential for a comprehensive record of deformation and metamorphism in HP metamafic rocks.

White mica is a common mineral in HP–LT-altered oceanic metamafic and metasedimentary lithologies and is stable throughout prograde and retrograde reactions (Schmidt et al., 2004; Halama et al., 2020). The high Rb contents and the estimated high closure temperature of the rubidium–strontium (Rb–Sr) system in this mineral (500 ± 50 °C; Jäger et al., 1967; von Blanckenburg et al., 1989; Villa, 1998; Glodny et al., 1998, 2008) make white mica a suitable geochronometer for dating subduction-related processes, especially when combined with low Rb/Sr phases. Despite the robustness of multimineral Rb–Sr isochron analyses (Glodny et al., 2004, 2008; Wawrzenitz et al., 2006; Bröcker et al., 2013; Kirchner et al., 2016; Angiboust and Glodny, 2020), significant challenges remain. These include (i) Sr isotope disequilibrium between micas and the other mineral phases; (ii) coexistence of several generations of micas; (iii) post-deformation, low-temperature magmatic alteration or fluid-assisted recrystallization; (iv) thermally induced diffusion processes (Glodny and Ring, 2022); and (v) potential inheritance within mica grains or across mica populations (Villa, 2016; Barnes et al., 2024). These variations in mica Rb–Sr systematics and isotopic variability can be directly addressed using in situ laser-ablation methods (e.g., Ribeiro et al., 2023b).

In situ Rb–Sr dating of white mica using laser-ablation triple-quadrupole inductively coupled plasma mass spectrometry (LA-ICP-MS/MS) offers significant advantages over conventional ID (isotope dilution) thermal ionization mass spectrometry (TIMS) analyses. This technique eliminates the need for mineral separation and time-consuming chromatographic column chemistry, enabling quick, cost-effective analyses. It further allows us to constrain potential zoning in Rb–Sr isotope distribution (Kutzschbach and Glodny, 2024; Rösel and Zack, 2022), hence preserving essential textural information that is otherwise lost. Thus, potential age variations among different white mica populations (e.g., syn- to post-kinematic grains) within distinct microstructural domains such as microfolds, shear zones, and boudin necks permit a more accurate interpretation of the resulting ages (Tillberg et al., 2020; Gou et al., 2022; Gyomlai et al., 2022, 2023a, b; Kirkland et al., 2023; Ribeiro et al., 2023a; Ceccato et al., 2024; Barnes et al., 2024). This method has been extensively applied to constrain the timing of deformation events in Precambrian–Paleozoic felsic lithologies (Olierook et al., 2020; Tillberg et al., 2021; Wang et al., 2022; Ribeiro et al., 2023), but its application remains limited in mafic lithologies. For example, a recent study on mafic blueschist from Syros (Greece) presented white-mica-only isochron ages interpreted to date fluid–rock interactions along the subduction interface (Gyomlai et al., 2023b). More accurate age constraints were obtained by combining Rb–Sr dating of white mica with initial Sr isotope constraints of epidote and apatite in metamafic rocks from Syros (Barnes et al., 2024).

These studies highlight the great potential of in situ mica Rb–Sr geochronology by LA-ICP-MS/MS to investigate different rock types and geological questions (e.g., Redaa et al., 2022; Wang et al., 2022; Zametzer et al., 2022; Huang et al., 2023; Giuliani et al., 2024). However, it remains challenging to date young (i.e., Cenozoic) metamafic and metasomatic lithologies with low Rb contents (e.g., < 30 ppm in mafic rocks) and associated low Rb/Sr micas where ingrowth of radiogenic Sr is limited. In this contribution, we address the limitations of in situ Rb–Sr dating of white mica in young metamafic and metasomatic rocks and propose strategies to obtain robust Rb–Sr ages using laser-ablation methods. We present new data of 10 samples from Syros (Kampos Belt and Megas Gialos area; Greece) and integrate petrographic and textural analysis of HP–LT rocks with laser-ablation Rb–Sr analyses of white mica and multi-collector (MC) ICP-MS Sr isotope analyses of epidote (complemented with bulk rock Sr isotopes for some of the samples). Although the general architecture and structural relationships of blueschist to eclogite-facies rocks on Syros are still debated (e.g., Keiter et al., 2011; Laurent et al., 2018; Kotowski et al., 2022), the subdivision of geological units, pressure–temperature (P-T) conditions, and the timing of metamorphic burial and exhumation are well constrained, making Syros an ideal case study for our purpose. We demonstrate that in these young (Cenozoic) metasomatic and metamafic rocks, anchoring mica-based Rb–Sr isochrons to initial (or "common") $^{87}Sr/^{86}Sr$ from a cogenetic phase such as epidote or a geologically meaningful "model" (e.g., Rösel and Zack,

2022) circumvents issues with low Rb–Sr ratios in these rocks.

2 Geological setting

Syros

The HP–LT rocks from Syros belong to the Cyclades Blueschists Unit (CBU) cropping out along the Aegean Sea (Fig. 1a and b). The CBU is interpreted to represent exhumed fragments of the subducted Adriatic plate and HP–LT metaophiolites of a northward-dipping subduction event between the Eurasian and African plates (Gautier and Brun, 1994; Jolivet et al., 2010; Soukis and Stockli, 2013). The CBU is subdivided into three subgroups (Glodny and Ring, 2022), from which the Top CBU and Middle CBU nappes are relevant for this study. The Top CBU nappe crops out on Syros as a narrow belt, known in the literature as the Kampos Belt, to which one of the study localities belongs to, i.e., the Grizzas shear zone (Fig. 1c). It is composed of abundant metavolcanic materials with a bimodal composition (mafic and felsic) along with metagabbros, serpentinites, tremolite–chlorite, talc and garnet schists (Keiter et al., 2011). The Kampos Belt lithologies reached peak blueschist to eclogite-facies conditions of 480–560 °C and 1.6–2.2 GPa (e.g., Trotet et al., 2001; Laurent et al., 2018; Cisneros et al., 2021). The Middle CBU nappe is the most abundant unit and is mainly composed of a relatively coherent intercalation of marbles, metasediments, and metabasites (Fig. 1b). This latter lithotype represents the studied lithology at the Megas Gialos locality (Fig. 1b and f), displaying a pervasive exhumation overprint transitioning from blueschist to greenschist-facies from 450 to 400 °C and 1.4 to 1.0 GPa (Cisneros et al., 2021). These retrograde metamorphic conditions are associated with transient brittle fracturing and dilational veining (Muñoz-Montecinos and Behr, 2023), from which the investigated samples from Megas Gialos were collected.

The pre-subduction architecture of the CBU resulted from Triassic rifting of the basement accompanied by deposition of passive margin sediments and carbonates (Keay, 1998; Seman et al., 2017). Rifting occurred at ca. 80 Ma, thinning the lithosphere and producing small-scale oceanic basins along with passive margin depocenters (Keiter et al., 2011; Cooperdock et al., 2018; Kotowski et al., 2022). In the Kampos Belt (Grizzas locality), U–Th–Pb SHRIMP zircon analyses in a metagabbro and a meta-plagiogranitic dike reveal two age populations, one at ca. 80 Ma and one at 52.4 ± 0.8 Ma (Tomaschek et al., 2003). The older age likely reflects the magmatic crystallization, whereas the younger one dates the HP–LT peak metamorphism. Phengite and multi-mineral Rb–Sr (e.g., white mica + epidote + glaucophane +/− omphacite +/− garnet), phengite Ar–Ar and garnet Lu–Hf ages (mostly from the Lia side, hereafter referred to as the western Kampos Belt) are in the range of 55 to 44 Ma and were interpreted to reflect the timing of prograde-to-peak HP–LT metamorphism (see Kotowski et al., 2022, and references therein). Similar peak ages of 51.8 ± 0.1 Ma were obtained by Lu–Hf geochronology of garnet in a metasedimentary rock from the Fabrikas outcrop in southern Syros (Tual et al., 2022). The initial stage of exhumation under blueschist-facies conditions likely began at ca. 44 Ma and transitioned to greenschist-facies conditions between 34 and 20 Ma based on Ar–Ar and Rb–Sr multi-mineral (e.g., white mica + epidote + albite) geochronology (e.g., Putlitz et al., 2005; Uunk et al., 2018; Glodny and Ring, 2022, and references therein). Gyomlai et al. (2023b) obtained three in situ mica Rb–Sr ages from an outcrop within the Kampos Belt (Lia side) in the range of 36.3 ± 5.1 to 36.1 ± 4.7 Ma, inferred to date metasomatism of metamafic rocks during blueschist- to greenschist-facies exhumation. The authors also reported older ages in the range of 52.5 ± 11.6 to 39.8 ± 7.4 Ma (Kampos Belt, Lia side), but it is unclear whether these ages represent metasomatism and/or mineral (re)crystallization during peak metamorphism or retrogression during HP to late exhumation. Multi-mineral and in situ white mica Rb–Sr and Ar–Ar dating in the Middle CBU nappe yielded peak HP–LT metamorphism ages of 45 to 37 Ma, whereas the pervasive blueschist to greenschist-facies metamorphism is dated at ca. 39 to 19 Ma (Glodny and Ring, 2022; Barnes et al., 2024; Kotowski et al., 2022, and references therein).

3 Samples and petrography

In this section, we present key petrographic observations of the 10 samples from Syros that have been selected for Rb–Sr dating (Table 1), emphasizing the textural context of white mica and epidote. Two additional samples (SYGR50 and SYGR44) have been analyzed for epidote $^{87}Sr/^{86}Sr$ only. The investigated samples were carefully selected in order to constrain the timing of fluid–rock interaction (metasomatism and veining) and to evaluate the significance of $^{87}Sr/^{86}Sr$ isotopic values for anchoring white mica Rb–Sr isochrons. We targeted our samples based on the presence of white mica in apparent textural equilibrium with epidote (where present) and, for the Grizzas samples, the apparent absence of greenschist-facies overprinting.

The samples coded SYGR (seven out of nine samples were dated) all belong to the Grizzas locality in the easternmost part of the Kampos Belt (Fig. 1b and c). These samples were collected along a north-dipping shear zone (hereafter referred to as the Grizzas shear zone), which juxtaposes a massively to variably strained metagabbro and blueschist-facies igneous breccia, representing a region of high and localized strain (Fig. 1c; see also Keiter et al., 2011). Samples SYGR36 and SYGR44 correspond to relict (partially digested) blueschist blocks, while sample SYGR50 represents a pristine, low-strain metagabbro. SYGR37 and SYGR38 represent the metasomatized mafic matrix wrapping around

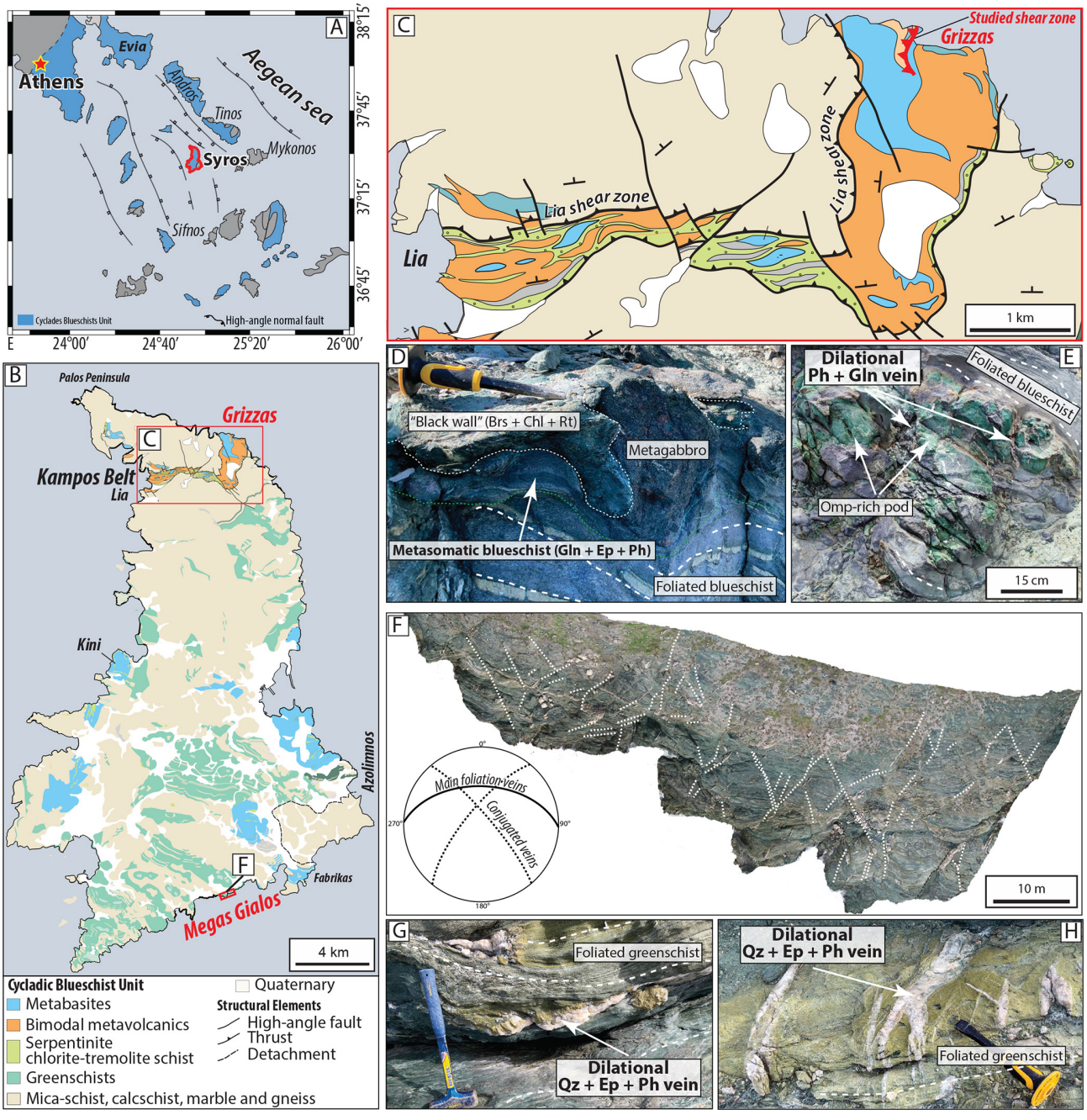

Figure 1. **(a)** Simplified geologic map of the Cyclades highlighting the location of Syros. **(b)** Simplified geologic map of Syros (modified from Keiter et al., 2011). The study localities are highlighted in red. **(c)** Zoom in of the Kampos Belt. The study locality is shown in red. **(d)** Field image of an omphacitite pod embedded in a foliated blueschist matrix within the Grizzas shear zone; the former contains some of the studied glaucophane + phengite dilational veins (sample SYGR41). **(e)** Representative field image of metasomatic rocks from the Grizzas shear zone; note the occurrence of smeared metagabbro blocks surrounded by metasomatic rinds and black walls within a foliated blueschist and a chlorite–tremolite schist matrix. **(f)** Orthomosaic image from the Megas Gialos outcrop (inset from panel **b**; modified from Muñoz-Montecinos and Behr, 2023). The lower-hemisphere stereoplot depicts the orientation of the veins following the main foliation and those sets oblique to it (dashed white lines illustrate the orientation of conjugated vein sets), represented here by samples SYMG08.3 and SYMG02, respectively. Panels **(g)** and **(h)** are examples of dilational veins containing epidote fibers along with phengite.

the metagabbro and blueschist blocks (i.e., metasomatic rinds in Fig. 1d), whereas sample SYGR42 is an altered metagabbro (see Table 1 for a summary of the studied samples). For comparison, a metasedimentary rock sample (SYGR45) from a ∼ 70 cm thick discrete layer within the shear zones and a felsic pod (sample SYGR58) contained within a moderately strained meta-igneous breccia (e.g., Keiter et al., 2011) were also targeted for dating. We emphasize the occurrence of dilational phengite + glaucophane veins (such as sample SYGR41) crosscutting omphacitite pods (Fig. 1e). The samples coded SYMG were collected from a retrograde greenschist to blueschist-facies sliver located in the Megas Gialos locality (Fig. 1f). The selected vein samples SYMG02 and SYMG08.3 (Fig. 1g and h) formed as dilational fractures related to the ascent of deep subduction zone fluids towards the base of the fore arc during the latest stages of HP–LT exhumation and extension (e.g., Muñoz-Montecinos and Behr, 2023). Sample SYMG07 represents the greenschist host rock associated with the vein samples SYMG02 and SYMG08.3.

3.1 Blueschists, blueschist-facies metagabbro, and greenschist

Samples SYGR36 and SYGR44 are relict blueschist blocks within a metasomatized sheared matrix. Glaucophane, together with white mica and epidote, define the penetrative foliation. Texturally, white mica occurs as medium-grained laths and displays no evidence of kinks, undulose extinction, or fish. In sample SYGR36, white mica also occurs within pressure shadows (Fig. 2a) and boudin necks around garnet and oblique to the main foliation. No significant zoning patterns in major elements were observed (Fig. S1a–f in the Supplement; see also Fig. S2 for white mica mineral chemistry data). Mostly, white mica grains defining the main foliation and those spatially related to pressure shadows were targeted for dating. Sample SYGR44 texturally preserves lozenge-shaped lawsonite pseudomorphs now composed of strain-free epidote (targeted for $^{87}Sr/^{86}Sr$ analyses) and white mica (Fig. S1g).

Sample SYGR50 is a low-strain metagabbro composed of coarse-grained clinopyroxene pseudomorphs (now glaucophane, winchite, and omphacite) in a matrix of epidote. The (weak) foliation is defined by elongated tabular crystals of epidote and subordinate white mica. Boudin necks within large porphyroclasts are filled by epidote, white mica, and garnet (Fig. S1h). In this sample, epidote crystals defining the foliation and filling the boudin necks were targeted for $^{87}Sr/^{86}Sr$ analyses. Overall, this sample represents the weakly metasomatized analogue of the altered metagabbro sample SYGR42.

Sample SYMG07 is a coarse-grained greenschist and represents the host rock associated with the vein samples SYMG02 and SYMG08.3. The main foliation is defined by amphibole and epidote, oriented laths of chlorite and white mica, and stretched albite (Fig. 2b). Phengite grains in the matrix exhibit weak core–mantle zoning patterns noticeable in backscattered electron imaging, reflecting mild variations in $Mg^{2+}/(Fe^{2+} + Mg^{2+})$ ratios (XMg) (Fig. S1b; see also Fig. S2). The core of large white mica grains was targeted for dating, while the foliated matrix epidote was targeted for $^{87}Sr/^{86}Sr$ determinations since these are interpreted as part of an equilibrium assemblage.

3.2 Metasomatic rinds, altered metagabbro, and veins

Samples SYGR37 and SYGR38 represent the matrix wrapping around metagabbro and blueschist blocks. These samples are coarse-grained, foliated schists composed mainly of glaucophane, epidote, phengite, and chlorite. White mica from both metasomatic rinds are medium- to coarse-grained and occur in sharp contact with glaucophane and epidote, displaying no significant chemical zoning patterns in major elements or textural evidence of recrystallization (Fig. 2c and d; see also Fig. S2). Sharp contacts between white mica and epidote suggest textural equilibrium between them (Fig. S1c). Thus, we targeted these microdomains for white mica dating and $^{87}Sr/^{86}Sr$ determinations.

Sample SYGR42 is an altered metagabbro composed of porphyroclasts of Na–Ca amphibole and omphacite after igneous clinopyroxene in a matrix of epidote, white mica, and glaucophane (Fig. 2e). Two generations of epidote, spatially associated with two distinct microdomains, are observed. The first epidote generation grew as fine-grained and now heavily smeared crystals occupying the interstitial matrix between porphyroclasts. This texture likely reflects epidote growth after igneous plagioclase and subsequent deformation. The second epidote generation grew in microdomains where a discontinuous foliation composed of tabular glaucophane and epidote in sharp contact with white mica, wrapped around porphyroclasts and the fine-grained epidote matrix. Within this second microdomain, white mica is medium- to coarse-grained and displays evidence of recrystallization and subgrains. For this reason, coarse-grained white mica crystals displaying no textural evidence for recrystallization, such as subgrains, kinks, and undulose extinction, were carefully selected for dating, whereas euhedral and tabular epidote crystals in sharp contact with white mica crystals were targeted for $^{87}Sr/^{86}Sr$ analysis.

Sample SYGR41 is a glaucophane + white mica dilational vein crosscutting an omphacitite pod. These veins display up to centimeter-sized and randomly oriented laths of white mica (Fig. 2f) displaying no evidence of deformation or significant chemical zoning (Fig. S1d).

Samples SYMG02 and SYMG08.3 are dilational veins crosscutting the foliated greenschist hosts. Elongated epidote crystals occur spatially associated with white mica in sharp contact, suggesting contemporaneous precipitation from a fluid phase (Fig. 2g and h). White mica occurs as euhedral, laths that are hundreds of micrometers long and correspond to strain-free crystals with no to faint chemical zoning

Table 1. Summary of the samples selected for this study and their corresponding rock type, mineral assemblage (major minerals), and analyzed microdomains. Mineral abbreviations are from Whitney and Evans (2010). Ab is albite, Act is actinolite, Chl is chlorite, Ep is epidote, Gln is glaucophane, Grt is garnet, Lws is lawsonite, Omp is omphacite, Qz is quartz, Rt is rutile, Ttn is titanite, Tur is tourmaline, Wm is white mica, and Wnc is winchite.

Sample ID	Rock type and general structure	Mineral assemblage	Analyzed microdomain
Grizzas shear zone (NE Syros)			
Blueschist-facies			
SYGR36	Strongly foliated blueschist block	Gln + Ep + Wm + Grt + Omp + Rt	Wm defining the main foliation and pressure shadows around Grt
SYGR37	Moderate to strongly foliated metasomatic rind	Gln + Ep + Wm + Chl	Wm defining the main foliation
SYGR38	Weakly foliated metasomatic rind	Gln + Ep + Wm + Chl	Randomly oriented and interlocked Wm and Ep
SYGR41	Dilational vein	Gln + Wm	Randomly oriented laths of Wm
SYGR42	Moderately foliated metagabbro	Gln + Wnc + Omp + Ep + Wm + Rt	Shear bands defining the main foliation
SYGR44	Moderately foliated blueschist block	Gln + Lws (now Ep + Wm) + Wm + Grt + Rt	Ep replacing Lws pseudomorphs
SYGR45	Foliated metasediment	Wm + Gln + Grt + Ep + Tur	Wm aligned and oblique according to the main foliation
SYGR50	Weakly to moderately foliated metagabbro	Omp + Ep + Gln + Wm	Ep defining the main foliation and within boudin necks
SYGR58	Moderately foliated felsic pod	Qz + Wm	Wm aligned and oblique according to the main foliation
Megas Gialos (SE Syros)			
(HP) Greenschist-facies			
SYMG02	Dilational vein	Qz + Ep + Wm + Ab	Ep fibers and Wm laths in close contact
SYMGG07	Moderately to strongly foliated	Ep + Ab + Chl + Act + Wm + Ttn	Ep and Wm defining the main foliation
SYMG08.3	Dilational vein	Qz + Ep + Wm	Ep fibers and Wm laths in close contact

(Fig. S1e and f). Thus, the most coarse and pristine (e.g., unfractured) crystals were selected for white mica dating and epidote $^{87}Sr/^{86}Sr$ analyses.

3.3 Metasedimentary rock and felsic pod

Sample SYGR45 is a well-foliated garnet, glaucophane, tourmaline, and mica schist with minor epidote (Fig. 2i). Texturally, the foliated white mica generation is apparently overgrown by a second, static generation characterized by laths oriented oblique to the main foliation (Fig. 2e). To avoid potentially retrograde rims, cores of large crystals defining the pervasive foliation and those of crystals oblique to it were targeted for dating. However, the resulting ages for these two white mica generations were indistinguishable within uncertainty; therefore, the final age for this sample was calculated by clustering both datasets (see below).

Sample SYGR58 is a felsic pod contained within the blueschist-facies meta-igneous breccia. They are composed mostly of quartz and phengite and subordinate epidote and garnet, the latter typically replaced by chlorite. A first white mica generation defines the foliation, whereas a second generation of laths is oriented oblique to it (Fig. 2j). Although the two white mica generations were separately targeted for dating, the resulting ages overlap and were merged for the final sample age calculation (see below).

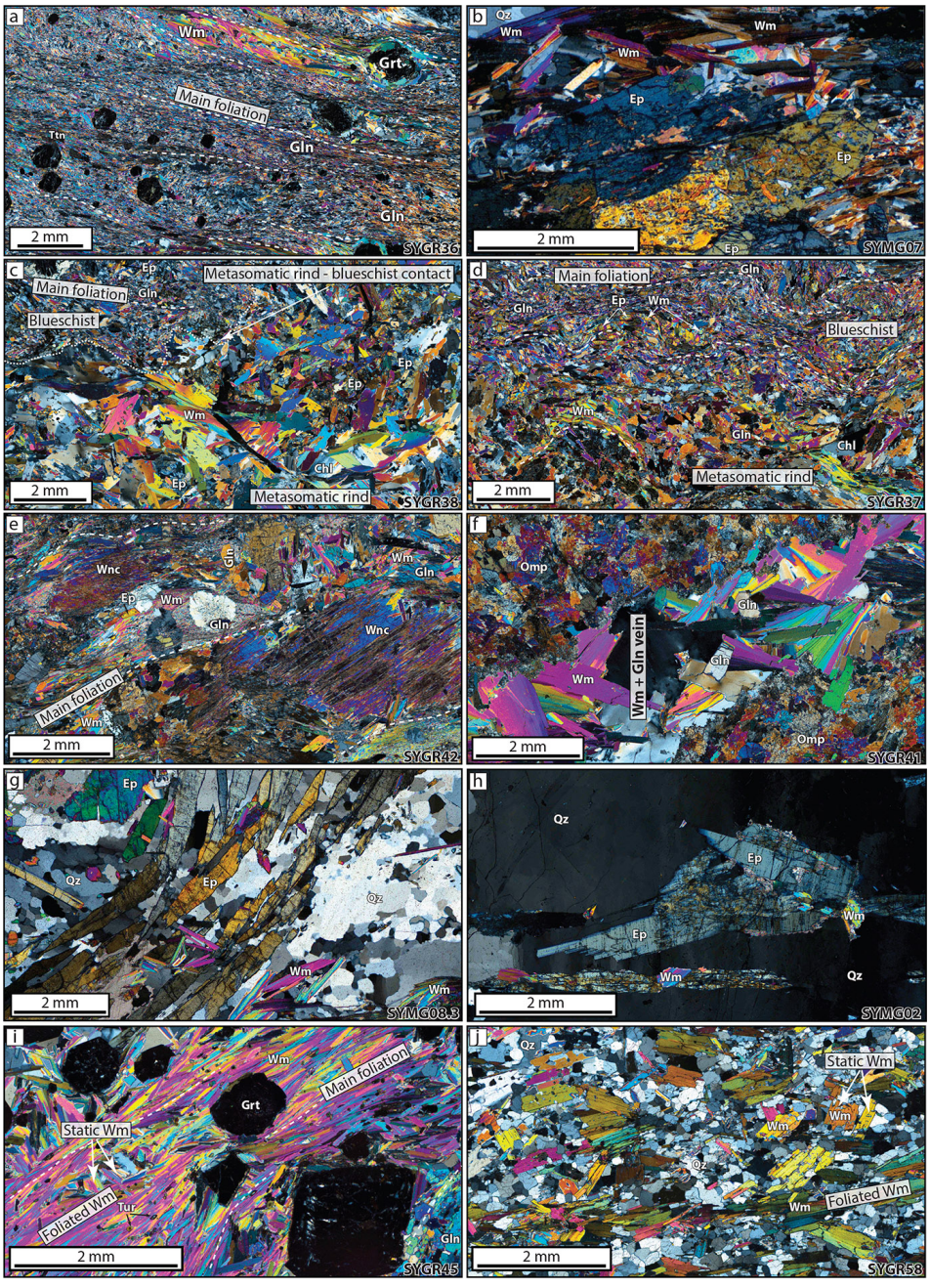

Figure 2. Photomicrographs (crossed polars) of the dated samples. **(a)** General overview of the blueschist block sample SYGR36 emphasizing the distribution of white mica along the foliation and typically around garnets forming pressure shadows. **(b)** General fabric of the greenschist sample SYMG07 displaying the association between foliated epidote and white mica. Due to the significant amount of inclusions within epidote, only the inclusion-free regions were targeted for laser-ablation MC-ICP-MS analysis. **(c)** Contact between altered blueschist and metasomatic rind in sample SYGR38; note the relatively curvy and sharp contact between these two domains and the relatively large abundance of coarse-grained white mica in the latter. **(d)** Contact between altered blueschist and metasomatic rind in sample SYGR37. In this case, the contact is moderately to highly strained, resulting in a more diffuse appearance. **(e)** Metasomatized metagabbro sample SYGR42 displaying clinopyroxene pseudomorph porphyroclasts (now replaced by amphibole) in a foliated matrix composed of white mica, glaucophane, and epidote. **(f)** Dilational vein crosscutting an omphacitite pod (sample SYGR41) with strain-free, millimeter-sized white mica crystals in association with glaucophane. **(g)** Dilational white mica + epidote + quartz vein (sample SYMG08.3) with a texture characterized by epidote fibers and white mica laths. **(h)** Dilational white mica + epidote + quartz vein (sample SYMG02) displaying coarse-grained epidote in sharp contact with finer-grained white mica. **(i)** Metasedimentary rock sample SYGR45 highlighting white mica crystals oriented parallel and oblique (static) to the main foliation and developing pressure shadows around garnet. **(j)** Felsic pod sample SYGR58 highlighting the distribution of white mica along the main foliation and some grains oriented oblique to it in a matrix of quartz.

4 Methods

4.1 Laser-ablation MC-ICP-MS

In situ Sr isotope analyses of epidote were undertaken in two separate sessions (March 2023 and February 2024) using an ASI RESOlution 193 nm excimer laser-ablation system interfaced to a Nu Plasma II MC-ICP-MS at ETH Zürich following a similar approach from Fitzpayne et al. (2023) and Pimenta Silva et al. (2023). Analytical conditions included 80–100 µm spot size, a repetition rate of 5 Hz (March 2023) and 10 Hz (February 2024), and laser fluence of ~ 4.0 (March 2023) and 2.5 J cm^{-2} (February 2024). Each analysis consisted of a sequence of 40 s of ablation and 15 s of washout followed by 30 s of gas blank measurement. Total Sr signals varied widely from ~ 1 to 15 V depending on the sample (Table S1 in the Supplement). Data reduction, including corrections for isobaric interferences (Kr, Ca dimers, Ca argides, Rb) and instrumental mass bias was performed using Iolite 4 (Paton et al., 2007, 2011). Instrumental drift was evaluated by repeated measurement of clinopyroxene BB-1 (Neumann et al., 2004; Fitzpayne et al., 2020), which was ablated every block of 15 unknowns including secondary clinopyroxene standards (JJG1414; YY09-04; YY09-47; YY12-01) from Zhao et al. (2020) (results included in Table S1). All data are reported relative to BB-1 of $^{87}Sr/^{86}Sr$ of 0.704468 (Fitzpayne et al., 2020) via standard bracketing. $^{84}Sr/^{86}Sr$ of clinopyroxene standards and epidote unknowns are generally within uncertainty of the natural ratio (~ 0.0565). $^{87}Rb/^{86}Sr$ ratios are negligible (typically < 0.001), which makes corrections for ^{87}Sr ingrowth insignificant. Therefore, the reported Sr isotope ratios are considered to be equal to the initial Sr isotope ratios at time of epidote crystallization.

4.2 Laser-ablation ICP-MS/MS

In situ Rb–Sr isotopic analyses of white mica in the thin section were undertaken during two sessions (October 2022 and May 2023) using an ASI Resolution 193 nm excimer laser probe interfaced to an Agilent 8800 ICP-MS/MS at ETH Zürich following the procedure outlined in Giuliani et al. (2024) and Ceccato et al. (2024), which builds upon the pioneering work of Zack and Hogmalm (2016) and Hogmalm et al. (2017). The mass spectrometer was first tuned in single-quad mode (i.e., no gas in the collision cell) to optimize the Rb and Sr signals by ablating NIST612. Oxide production rate based on measurement of ThO/Th in NIST612 was ≤ 0.2 %. After introducing ultrapure N_2O gas (> 99.99 %) into the reaction cell (flow rate of 0.23–0.25 mL min^{-1}), a second tuning step was undertaken by ablating NIST610 to maximize production of SrO^+ ions while maintaining high sensitivity for Rb^+ ions. Interaction of Sr^+ ions with N_2O resulted in conversion of ~ 89 % of Sr^+ ions to SrO^+ based on monitoring of masses 88 (Sr^+), 104 (SrO^+), and 105 ($SrOH^+$). No RbO^+ was detected. Analytical conditions for mica analyses included 80–100 µm spot size, pulse rate of 5 Hz, and laser fluence of ~ 3.5–4.0 J cm^{-2}. Each analysis consisted of a sequence of 40 s of ablation and 15 s of washout followed by 30 s of gas blank measurement. Dwell times were of 100 ms for ^{85}Rb, $^{86}Sr^{16}O$, and $^{87}Sr^{16}O$; 50 ms for ^{86}Sr and $^{87}(Sr + Rb)$; 20 ms for ^{88}Sr, $^{88}Sr^{16}O$, and $^{88}Sr^{16}OH$; and 10 ms for other elements (e.g., Ca, Ti, Ni, Ce, Yb, Th), which were monitored to assess potential contamination by extraneous material. Data reduction was performed using the "Rb–Sr isotopes" data reduction scheme in Iolite 4 (Paton et al., 2011). Instrumental drift and quantification of $^{87}Sr/^{86}Sr$ and "uncorrected" $^{87}Rb/^{86}Sr$ were undertaken by repeated ablation of NIST610, which was measured every block of 15 unknowns including in-house mica standards (see below). Natural glass standards BCR-2G and BHVO-2G were also analyzed as a quality measure of the Sr isotope analyses and returned values broadly consistent with accepted values (Table S2). NIST610 is a synthetic glass with different ablation properties than mica and, therefore, this approach provides biased (i.e., "uncorrected") $^{87}Rb/^{86}Sr$ ratios in mica analyses (e.g., Redaa et al., 2021). Correction of NIST610-based "uncorrected" $^{87}Rb/^{86}Sr$ in the mica unknowns was performed following the method outlined by Giuliani et al. (2024). The calculated age of an in-house mica standard from the Wimbledon kimberlite (South Africa), which has a robustly constrained Rb–Sr age of 114.5 ± 0.8 Ma (2σ) based on isotope dilution analyses (Sarkar et al., 2023) and exhibits large variation in Rb/Sr (almost 3 orders of magnitude), was employed to calculate a correction factor that is then employed to obtain the final $^{87}Rb/^{86}Sr$ in the mica unknowns. The validity of this approach was confirmed by analyses of micas from the Bultfontein kimberlite (South Africa) and Mount Dromedary monzonite (MD-2; Australia), which returned Rb–Sr ages that are indistinguishable from solution mode Rb–Sr and Ar–Ar analyses of mica on the same sample: 88.3 ± 0.2 Ma (Fitzpayne et al., 2020) and 99.20 ± 0.08 Ma (Phillips et al., 2017), respectively (Table S2). Time-resolved spectra of mica unknowns and reference materials were screened to remove anomalous regions based on, e.g., low concentrations of Rb and high concentrations of Sr, Ca, Ce, and/or other incompatible trace elements. Analyses with total signals of less than 10 s (after screening) and with anomalously low contents of Rb or high contents of Sr (and Ca), often resulting in $^{87}Rb/^{86}Sr < 2.5$, as well as analyses with large $^{87}Sr/^{86}Sr$ uncertainties and data points that plotted distinctly off the isochron, were not included in the Nicolaysen diagrams (Table S3). All the isochron ages were calculated using IsoplotR (Vermeesch, 2018) and the ^{87}Rb decay constant of 1.3972×10^{-11} a^{-1} (Villa et al., 2015). Trace element concentrations were not quantified.

5 Results

5.1 Epidote Sr isotopes

The $^{87}Sr/^{86}Sr$ ratios were measured by laser-ablation MC-ICP-MS in 5 of the 10 samples employed for mica Rb–Sr geochronology. Two additional samples (SYGR44; SYGR50) were also included to corroborate the signature of the blueschist and metagabbro rocks. For comparison, we also present isotope-dilution Sr isotope data in samples from the Megas Gialos locality, including the three samples analyzed for epidote and mica Rb–Sr isotopes. A summary of the new and available Sr isotope data for epidote is reported in Fig. 3, and the full datasets, including bulk rock Sr and Nd isotopic compositions, are included in Tables S1 and S4.

At Grizzas (Kampos Belt), the two blueschist samples (SYGR36 and 44) show very small ranges in epidote $^{87}Sr/^{86}Sr$ compositions (see Fig. S3) with indistinguishable weighted means of 0.70805 ± 0.00006 (2 SE; $n = 12$) and 0.70802 ± 0.00005 (2 SE; $n = 18$; Table 2 and Fig. S3). The other two Grizzas samples (the metasomatic rind SYGR38 and the metagabbro SYGR50) exhibit larger isotopic variability. The $^{87}Sr/^{86}Sr$ in sample SYGR38 varies widely between 0.70426 ± 0.00008 and 0.710002 ± 0.00008 ($n = 22$) with no statistically distinct populations (Fig. 3). The weighted mean (although statistically meaningless) is similar to those of SYGR36 and SYGR44: 0.70767 ± 0.00058. In sample SYGR50, 16 epidote grains parallel to the foliation yield a restricted range in Sr isotope values corresponding to a weighted mean of 0.70460 ± 0.00004, which is substantially less radiogenic than the blueschist samples from Grizzas, although it is similar to the lowest $^{87}Sr/^{86}Sr$ of sample SYGR38. Four epidote grains within boudin necks of sample SYGR50 show more radiogenic values of up to 0.70585 ± 0.00020.

Epidote in the three samples from Megas Gialos show very limited within-sample $^{87}Sr/^{86}Sr$ variability with weighted means of 0.70466 ± 0.00004 ($n = 24$) for SYMG02; 0.70534 ± 0.00005 ($n = 25$) for SYMG07 and 0.70520 ± 0.00005 ($n = 31$) for SYMG08.03 The epidote Sr isotope compositions are not correlated with the lithology as the greenschist sample SYMG07 has the same $^{87}Sr/^{86}Sr$ as one of the two dilational veins (SYMG02 and 08.03). Measured (i.e., present-day) $^{87}Sr/^{86}Sr$ of bulk rock SYMG07 is 0.705414 ± 0.000008 (2σ SD of NBS987 standards measured in the same session), marginally more radiogenic than the SYMG07 epidote and minimally affected by radiogenic ingrowth (e.g., ~ 0.0002 in 50 Myr) due to low bulk rock $^{87}Rb/^{86}Sr$ of 0.290 (Table S1). The bulk rock $^{87}Sr/^{86}Sr$ of SYMG08.03 (0.705281 ± 0.000006) is almost indistinguishable from the epidote value reported above. The very low $^{87}Rb/^{86}Sr$ (0.073) suggests minimal radiogenic Sr ingrowth in this bulk sample.

5.2 Mica Rb–Sr dating

In this section we report the mica Rb–Sr isotope data and describe the related isochronous array for each sample, complemented in five cases by epidote Sr isotope results. The complete white mica dataset, including Rb and Sr isotope ratios, is provided in Table S3 (see Table 2 for a summary of the age data). For each sample we also provide a model age where the mica Rb–Sr isochron is anchored to an assumed $^{87}Sr/^{86}Sr$ value, that is 0.7080 ± 0.0005 for all the samples from Grizzas, and 0.7050 ± 0.0005 for those from Megas Gialos. For Grizzas, employing this value is justified by the fact that the weighted mean of epidote Sr isotopes are ~ 0.708 for three of the four analyzed samples (Fig. 3; see also the compiled data in Fig. 3 for metabasites from the Top CBU), and "unanchored" mica Rb–Sr isochrons are generally within uncertainty of this value (see below). The epidote and bulk rock compositions at Megas Gialos cluster at $^{87}Sr/^{86}Sr$ of ~ 0.705 (Fig. 3) hence provide a robustly constrained initial Sr composition for anchoring the mica-based Nicolaysen arrays. In the Sect. 6, we will address the impact of changing initial (or "common") $^{87}Sr/^{86}Sr$ composition in the calculated Rb–Sr isochron.

5.2.1 SYGR36

White mica in the blueschist block sample SYGR36 shows a spread in $^{87}Rb/^{86}Sr$ between 15 and 53 ($n = 43/45$) associated with variations in $^{87}Sr/^{86}Sr$ between 0.7166 and 0.7407 (Fig. 4a). The limited Rb/Sr spread results in a poorly defined "unanchored" isochron age of 29 ± 17 Ma (2 SE, MSWD = 0.89, initial $^{87}Sr/^{86}Sr = 0.7149 \pm 0.0062$). Anchoring the phengite Rb–Sr data to epidote from the same sample (weighted-mean $^{87}Sr/^{86}Sr = 0.70805 \pm 0.00006$) provides a rather different (although within uncertainty) and considerably more precise age of 47.2 ± 4.4 Ma (2 SE, MSWD = 0.96). Assuming a modeled initial $^{87}Sr/^{86}Sr$ of 0.7080 ± 0.0005 (1 s) provides an age of 46.9 ± 5.1 Ma (2 s, MSWD = 0.96), overlapping closely with the epidote-anchored isochron age.

5.2.2 SYGR37

White mica grains in the metasomatic rind sample SYGR37 show a slightly larger spread in $^{87}Rb/^{86}Sr$ (22–112, $n = 36/38$) and $^{87}Sr/^{86}Sr$ (0.7211–0.7676) compared to SYGR36, resulting in a more precise unanchored isochron age of 32.3 ± 7.5 Ma (MSWD = 0.51, initial $^{87}Sr/^{86}Sr = 0.7158 \pm 0.0059$; Fig. S4). Anchoring these mica Rb–Sr to modeled initial $^{87}Sr/^{86}Sr$ of 0.7080 ± 0.0005 (2 SE) yields an older age of 41.1 ± 3.1 Ma (MSWD = 0.66).

5.2.3 SYGR38

White mica in the metasomatic rind SYGR38 shows spreads between 22–90 and 0.7140–0.7771 for $^{87}Rb/^{86}Sr$

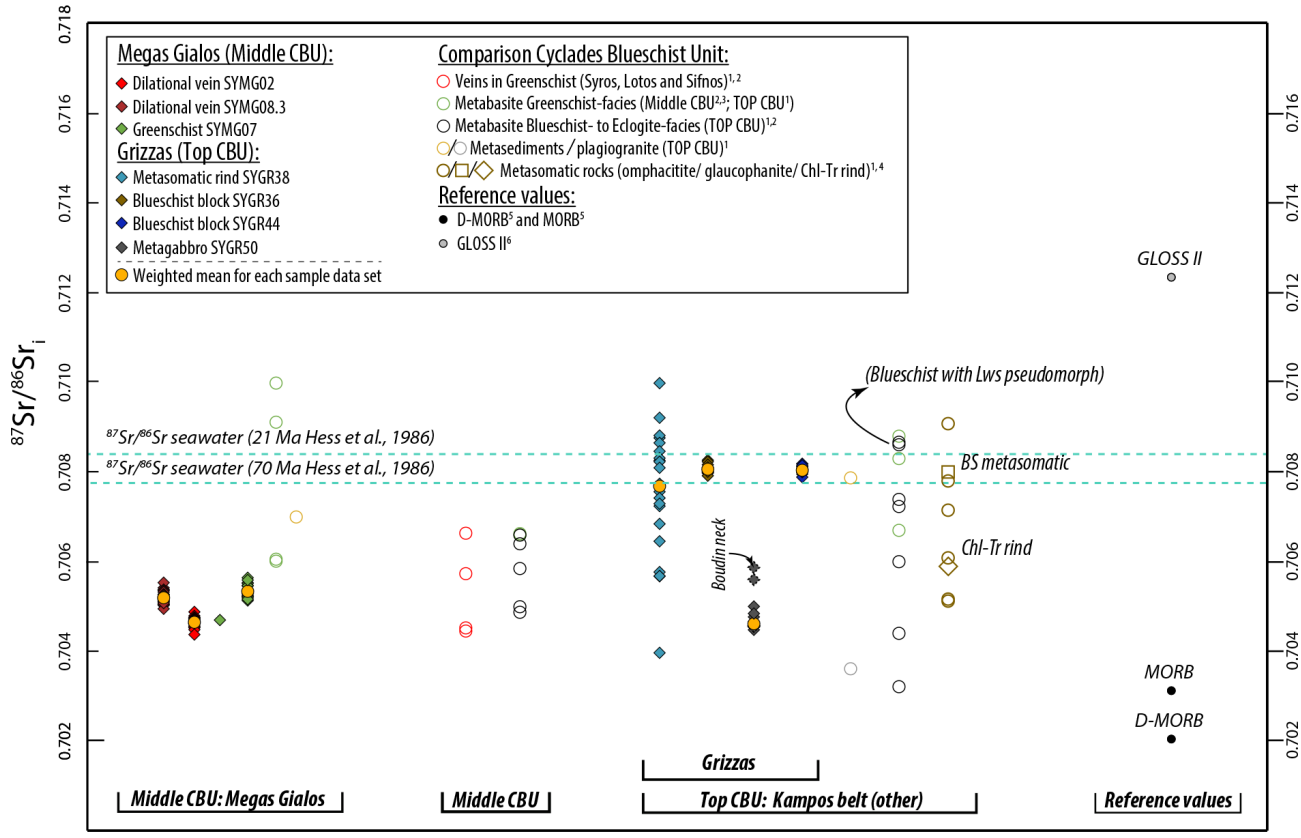

Figure 3. Overview of $^{87}Sr/^{86}Sr$ in situ laser-ablation MC-ICP-MS epidote data points and comparison to ID-TIMS (whole rock and multi-mineral) analyses from different localities on Syros. The resulting $^{87}Sr/^{86}Sr$ values are assumed to represent initial ratios due to the lack of Rb in epidote. For comparison, pristine MORB and D-MORB, compiled trench-filling sediments (GLOSS II), and Cretaceous to Miocene $^{87}Sr/^{86}Sr$ seawater values are shown. Uncertainties are smaller than the symbol size. In the figure, 1 is Glodny and Ring (2022); 2 is Kotowski et al. (2022); 3 is Bröcker et al. (2013); 4 is Bröcker and Enders (2001); 5 is Salters and Stracke (2004); and 6 is Plank (2014).

and $^{87}Sr/^{86}Sr$, respectively ($n = 20/25$, with five analyses excluded based on short signals of less than 10 s). The corresponding unanchored isochron age is 43 ± 10 Ma (MSWD = 0.6, initial $^{87}Sr/^{86}Sr = 0.7075 \pm 0.0064$; Fig. 4b). Adding epidote Sr isotopes (weighted-mean $^{87}Sr/^{86}Sr = 0.70767 \pm 0.00058$ (2 SE)) to the mica Rb–Sr isochron yields the same, yet more precise, age of 43.0 ± 5.4 Ma (MSWD = 0.54). Using a modeled initial $^{87}Sr/^{86}Sr$ of 0.7080 ± 0.0005 (2 SE) results in a similar age of 42.5 ± 5.5 Ma (MSWD = 0.54). Considering the large spread in epidote $^{87}Sr/^{86}Sr$ values (~ 0.7043 to ~ 0.7100), we have also calculated model ages using initial $^{87}Sr/^{86}Sr$ of 0.7050 and 0.7100, and these are within uncertainty of each other: 46.5 ± 5.6 Ma (MSWD = 0.57) and 39.8 ± 5.5 Ma (MSWD = 0.57), respectively (Fig. S5).

5.2.4 SYGR41

White mica from the dilational vein SYGR41 show a limited spread in $^{87}Rb/^{86}Sr$ between 14–63 ($n = 36/36$) associated with variations in $^{87}Sr/^{86}Sr$ between 0.7116 and 0.7498. An unanchored isochron through these data yields an age of 45 ± 11 Ma (MSWD = 0.78, initial $^{87}Sr/^{86}Sr = 0.7076 \pm 0.0049$). Anchoring these mica Rb–Sr data to a modeled initial $^{87}Sr/^{86}Sr$ of 0.7080 ± 0.0005 (1 s) yields the same, yet more precise, age of 44.7 ± 4.5 Ma (2 s, MSWD = 0.74).

5.2.5 SYGR42

The $^{87}Rb/^{86}Sr$ and $^{87}Sr/^{86}Sr$ ratios in phengites from the metasomatized metagabbro sample SYGR42 range from 27 to 185 and 0.7155 to 0.8162, respectively ($n = 30/30$), and the corresponding unanchored isochrons provide an age of 46 ± 9 Ma (MSWD = 1.3, initial $^{87}Sr/^{86}Sr = 0.7090 \pm 0.0079$). Anchoring these mica Rb–Sr data to $^{87}Sr/^{86}Sr = 0.7080 \pm 0.0005$ (1 s) results in an overlapping, although more precise, age of 46.6 ± 4.6 Ma (MSWD = 1.2).

5.2.6 SYGR45

Two generations of phengite laths, parallel and oblique to the main foliation, from the metasedimentary rock sample SYGR45 display $^{87}Rb/^{86}Sr$ values between 16 and 90 ($n =$

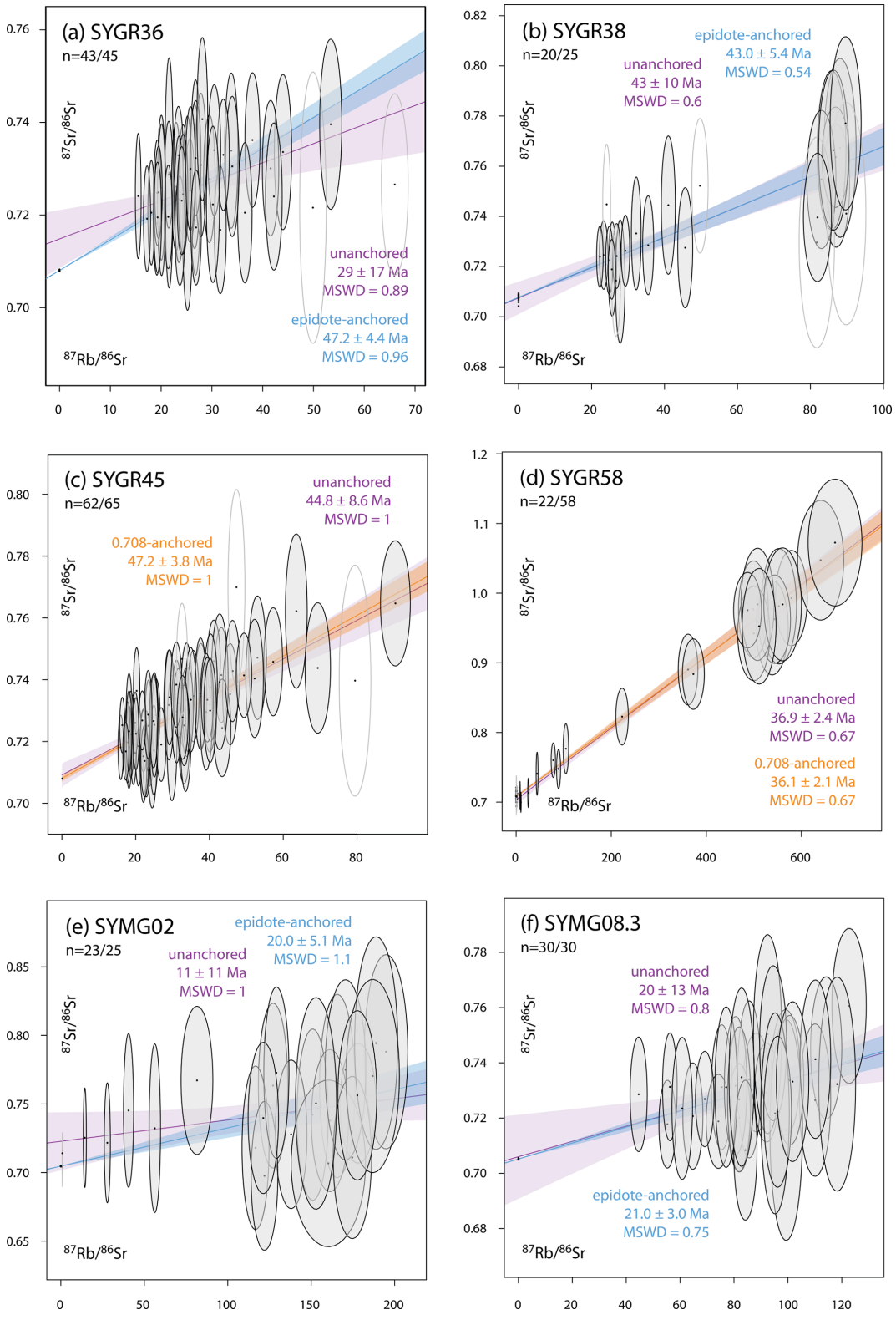

Figure 4. Representative laser-ablation ICP-MS/MS Rb–Sr isochrons of white micas from Grizzas (NE Syros, SYGR, **a–d**) and Megas Gialos (southern Syros, SYMG, **e–f**). The size of the ellipses represents internal 2 SE (standard error), where data points that were excluded from the regression are displayed as empty ellipses. Isochronous regressions are plotted together with their 95 % confidence level envelopes in different colors based on the employed anchoring technique: purple for mica-only unanchored regressions, blue for regressions anchored to epidote, and orange for regressions anchored to a modeled initial $^{87}Sr/^{86}Sr$ of 0.7080 ± 0.0005. The number below the sample labels indicates the number of mica analyses. All plots were generated using IsoplotR (Vermeesch, 2018).

62/65) and a corresponding variation in $^{87}Sr/^{86}Sr$ between 0.7134 and 0.7647, with no systematic difference between the two textural types of mica (Fig. 4c; Table S3). The resulting unanchored isochron has a slope equivalent to an age of 44.8 ± 8.6 Ma (MSWD = 1, initial $^{87}Sr/^{86}Sr = 0.7092 \pm 0.0038$). Anchoring these mica Rb/Sr data to a modeled initial $^{87}Sr/^{86}Sr$ of 0.7080 ± 0.0005 (1 s) yields a slightly older and more precise age of 47.2 ± 3.8 Ma (MSWD = 1), overlapping with the unanchored age within uncertainty. Using a more radiogenic initial $^{87}Sr/^{86}Sr$ of 0.7100 has a small effect on the calculated age (43.2 ± 3.8; MSWD = 1).

5.2.7 SYGR58

The two textural types of white mica identified in the felsic pod sample SYGR58, parallel and oblique to the main foliation, exhibit indistinguishable Rb–Sr isotope systematics (Table S3) and are hence described together. These white micas show the largest Rb/Sr spread observed in the sample set of between 8 and 671 ($n = 22/58$, where only analyses with $^{87}Rb/^{86}Sr > 2.5$ were considered for the isochron), which is consistent with the felsic nature of this sample. The spread in $^{87}Sr/^{86}Sr$ is between 0.670 and 1.073, resulting in precise, albeit unanchored, Rb–Sr age of 36.9 ± 2.4 Ma (MSWD = 0.67, initial $^{87}Sr/^{86}Sr = 0.7038 \pm 0.0072$; Fig. 4d). Anchoring these mica Rb/Sr data to a modeled initial $^{87}Sr/^{86}Sr$ of 0.7080 ± 0.0005 (2 SE) yields a similar age of 36.1 ± 2.1 Ma (2 s, MSWD = 0.67).

5.2.8 SYMG02

Phengites from the dilational vein sample SYMG02 show a relatively large $^{87}Rb/^{86}Sr$ spread between 14 and 195 ($n = 23/25$) associated with a restricted $^{87}Sr/^{86}Sr$ spread between 0.6976 and 0.7944. These data define a meaningless unanchored isochron (age = 11 ± 11 Ma, MSWD = 1, initial $^{87}Sr/^{86}Sr = 0.723 \pm 0.021$; Fig. 4e). Adding epidote Sr data from the same sample (weighted-mean $^{87}Sr/^{86}Sr = 0.70466 \pm 0.00004$) to the mica Rb–Sr isotopes results in a more meaningful age of 20.0 ± 5.1 Ma (MSWD = 1.1). Using a modeled initial $^{87}Sr/^{86}Sr$ anchor of 0.7050 ± 0.0005 (1 s) yields a similar age of 19.8 ± 5.2 Ma (2 s, MSWD = 1).

5.2.9 SYMG07

$^{87}Rb/^{86}Sr$ and $^{87}Sr/^{86}Sr$ values in white mica from the greenschist sample SYMG07 vary between 75–231 and 0.7199–0.8121, respectively ($n = 12/13$), yielding a meaningless isochron age of 6.1 ± 31.2 Ma (MSWD = 1.2, initial $^{87}Sr/^{86}Sr = 0.749 \pm 0.063$; Fig. S4). Coupling white mica with the SYMG07 epidote data (weighted-mean $^{87}Sr/^{86}Sr = 0.70534 \pm 0.00005$) results in an age of 27.2 ± 8.4 Ma (MSWD = 1.1). An identical age is obtained using a model initial $^{87}Sr/^{86}Sr$ of 0.7050 ± 0.0005 (1 s): 27.4 ± 8.4 Ma (2 s, MSWD = 1.2).

5.2.10 SYMG08

Phengites from dilational vein SYMG08.3 show a spread in $^{87}Rb/^{86}Sr$ between 45 and 123 ($n = 30/30$) associated with variations in $^{87}Sr/^{86}Sr$ between 0.7084 and 0.7606 (Fig. 4f). These data define an unanchored isochron age of 20 ± 13 Ma (MSWD = 0.8, initial $^{87}Sr/^{86}Sr = 0.706 \pm 0.015$). Adding Sr epidote data (weighted-mean $^{87}Sr/^{86}Sr = 0.70520 \pm 0.00005$) to the phengite Rb/Sr data results in the same, yet more precise, age of 21.0 ± 3.0 Ma (MSWD = 0.75). The results hardly change by anchoring the mica Rb/Sr data to a modeled initial $^{87}Sr/^{86}Sr$ of 0.7050 ± 0.0005 (2 SE): 20.8 ± 3.1 Ma (MSWD = 0.75) (Fig. S5).

6 Discussion

6.1 Optimal strategies to obtain robust Rb–Sr ages of white mica in young metamorphic rocks by LA-ICP-MS/MS

White mica in all of the investigated samples, regardless of their bulk rock chemistry (i.e., mafic and metasomatic), exhibits limited spread in Rb/Sr compared to previous studies (e.g., Kirkland et al., 2023; Glodny and Ring, 2022). Except for the relatively large spread observed in the felsic sample SYGR58 ($^{87}Rb/^{86}Sr = 8$ to 671), the Rb/Sr range of all the other samples never exceeds 1 order of magnitude and in some cases is even less (e.g., $^{87}Rb/^{86}Sr = 15$–53 in blueschist SYGR36) compared to, for example, the 2 to 3 orders of magnitude in phlogopite from lamproites and kimberlites (Giuliani et al., 2024) or biotite in some metamorphosed granites (Ceccato et al., 2024). In addition, the combination of relatively low Rb contents (not quantified but inferred from low Rb/Sr ratios) and geologically young (Cenozoic) age of the Syros micas did not allow the ingrowth of substantial radiogenic ^{87}Sr as shown by the low measured $^{87}Sr/^{86}Sr$ (generally < 0.8; Table S3). Low ^{87}Sr contents are associated with large uncertainties for $^{87}Sr/^{86}Sr$, which systematically exceed 1 % (2 SE) for individual measurements (Table S3). The compounded effects of low absolute $^{87}Rb/^{86}Sr$ values (generally < 200 and for some samples < 100), limited spread in Rb/Sr, and poor precision in the quantification of $^{87}Sr/^{86}Sr$ result in large uncertainties associated with the slopes of unanchored mica Rb–Sr isochrons (Fig, 5a and b). These uncertainties translate to a poor precision for the related ages, with 10 %–29 % RSE (relative standard error) in the SYGR samples (except for the felsic sample SYGR58, with an RSE of 3 %, i.e., 36.9 ± 2.4 Ma, 2 SE), and even larger uncertainties for the younger SYMG samples (Fig. 6a). The inverse correlation between relative $^{87}Rb/^{86}Sr$ spread and age uncertainty of unanchored isochrons in Fig. 5b exemplifies the impact of Rb/Sr variations on isochron precision. In at least three cases (SYGR36, SYMG02, and SYMG07) these unanchored mica-only isochronous arrays are not just imprecise but also rather inaccurate, as shown by

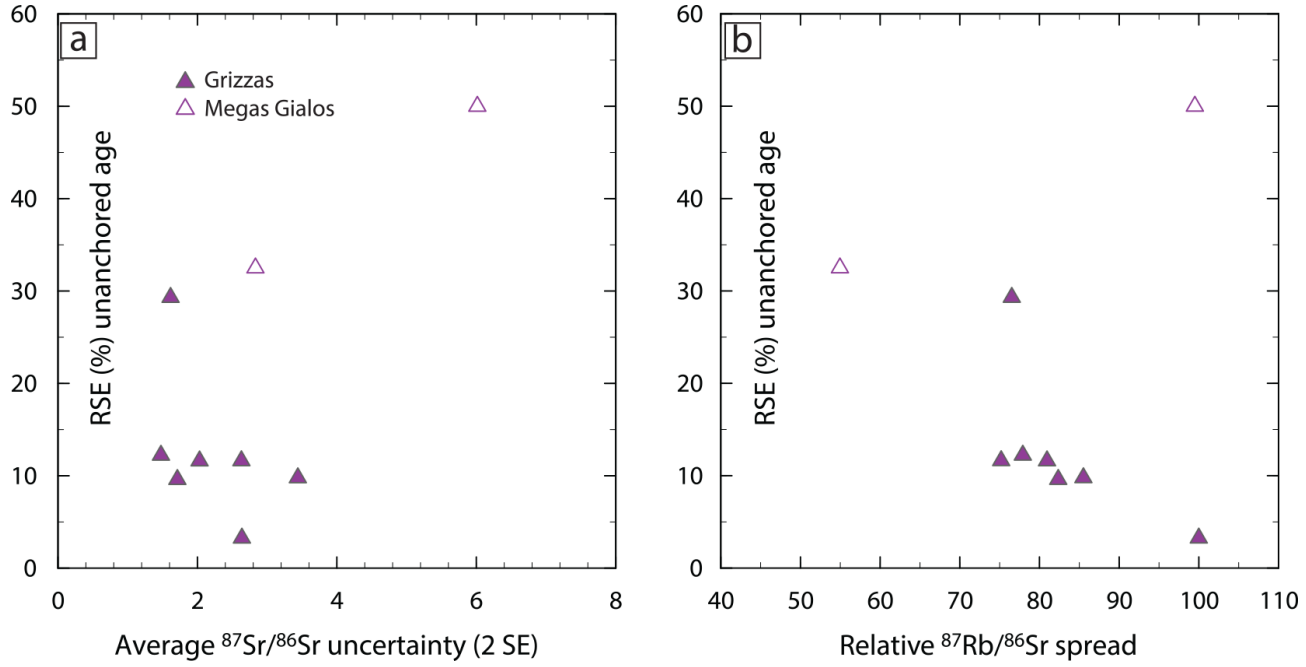

Figure 5. Comparison of relative standard error (RSE) of unanchored mica Rb–Sr ages and **(a)** average $^{87}Sr/^{86}Sr$ uncertainties and **(b)** relative (%) $^{87}Rb/^{86}Sr$ spread. The latter was defined as the ratio between the absolute $^{87}Rb/^{86}Sr$ spread and the highest $^{87}Rb/^{86}Sr$ value observed for any given sample, resulting in a number between 0 % and 100 %.

Table 2. Summary of epidote Sr isotopes and mica Rb–Sr ages. Ages are highlighted in bold.

Sample ID	Epidote $^{87}Sr/^{86}Sr$[a]			Mica analyses	Mica age, unanchored[b]				Mica + epidote age (Ma)			Mica age (Ma), anchored[c]		
	n	mean	2 SE	*n*	age (Ma)	2 SE	MSWD	isochron *y* intercept	age (Ma)	2 SE	MSWD	age (Ma)	2 SE	MSWD
Grizzas (NE Syros)														
SYGR36	12	0.70805	0.00006	43/45	**29**	17	0.89	0.7149 ± 0.0062	**47.2**	4.4	0.96	**46.9**	5.1	0.96
SYGR37	–	–	–	36/38	**32.3**	7.5	0.51	0.7158 ± 0.0059	**–**	–	–	**41.1**	3.1	0.66
SYGR38	21	0.70767	0.00058	20/25	**43**	10	0.60	0.7075 ± 0.0064	**43.0**	5.4	0.54	**42.5**	5.5	0.54
SYGR41	–	–	–	36/36	**45**	11	0.78	0.7076 ± 0.0049	**–**	–	–	**44.7**	4.5	0.74
SYGR42	–	–	–	30/30	**46**	9	1.30	0.7090 ± 0.0079	**–**	–	–	**46.6**	4.6	1.2
SYGR44	18	0.70802	0.00005	–	**–**	–	–		**–**	–	–	**–**	–	–
SYGR45	–	–	–	62/65	**44.8**	8.6	1.00	0.7092 ± 0.0038	**–**	–	–	**47.2**	3.8	1
SYGR50	16	0.70460	0.00004	–	**–**	–	–		**–**	–	–	**–**	–	–
SYGR58	–	–	–	22/58	**36.9**	2.4	0.67	0.7038 ± 0.0072	**–**	–	–	**36.1**	2.1	0.67
Megas Gialos (SE Syros)														
SYMG02	24	0.70466	0.00004	23/25	**11**	11	1.00	0.723 ± 0.021	**20.0**	5.1	1.1	**19.8**	5.2	1
SYMG07	25	0.70534	0.00005	12/13	**6.4**	31.2	1.20	0.749 ± 0.063	**27.2**	8.4	1.1	**27.4**	8.4	1.2
SYMG08.3	31	0.70520	0.00005	30/30	**20**	13	0.80	0.706 ± 0.015	**21.0**	3.0	0.75	**20.8**	3.1	0.75

[a] Laser-ablation multi-collector ICP-MS; the complete dataset is given in Table S1. [b] Laser-ablation ICP-MS/MS; the complete dataset is given in Table S3. [c] Anchoring values are 0.7080 ± 0.0005 for SYGR samples and 0.7050 ± 0.0005 for SYMG samples.

the substantially older ages of the mica + epidote isochron for SYGR36 (29 ± 17 Ma vs. 47.2 ± 4.4 Ma for SYGR36), or simply geologically meaningless (11±11 Ma and 6.4±31 Ma for SYMG02 and SYMG07, respectively; Table 2).

To overcome the limitations in mica Rb–Sr geochronology by LA-ICP-MS/MS due to low Rb/Sr and/or young ages, the two viable solutions explored here include anchoring the isochronous arrays to either the Sr isotope composition of a low Rb/Sr phase in textural equilibrium with mica, such as epidote, or an assumed $^{87}Sr/^{86}Sr$ value. The latter approach effectively provides a "model age" and, while previously explored by Rösel and Zack (2022), it is rigorously evaluated herein by a systematic comparison with initial Sr isotope constraints from epidote and bulk rocks. Anchoring mica isochrons to a low Rb/Sr phase has rarely been applied in mica Rb–Sr geochronology by LA-ICP-MS/MS (Ribeiro et al., 2022; Barnes et al., 2024; Giuliani et al., 2024), while being widely employed for conventional Rb–Sr dating by

isotope dilution (e.g., Glodny et al., 2008; Hyppolito et al., 2016; Angiboust et al., 2018; Dalton et al., 2020). Comparisons of unanchored mica Rb–Sr ages with those anchored using mean $^{87}Sr/^{86}Sr$ of epidote analyses show an improvement in precision of up to 6 times (Fig. 6b) and in some cases better accuracy, as shown above for SYGR36. Clearly, in young HP metamafic rocks such as those from Syros, this approach is recommended to obtain robust age constraints even when the limited spread in mica Rb/Sr prevents generation of meaningful isochronous arrays (i.e., SYMG02 and 07).

Model ages are also unsurprisingly substantially more precise than unanchored mica-only Rb–Sr ages. However, their accuracy deserves scrutiny. Where epidote data are available, the model ages calculated in this work can be employed to show the effect of inaccurate initial $^{87}Sr/^{86}Sr$ in the isochron ages (Fig. 7). At Grizzas, epidote $^{87}Sr/^{86}Sr$ varies between 0.7043 and 0.7100 (all of this variation is contained in the metasomatic rind sample SYGR38). Using available bulk rock data for the Kampos Belt (Fig. 3), this range can be extended downward to ~ 0.7030, effectively bracketing the possible compositions of initial Sr to calculate mica model ages. For simplicity, the same range is employed for Megas Gialos. Beyond the model ages presented in the results section and Table 2, for each sample two additional model ages are calculated using an initial $^{87}Sr/^{86}Sr$ of 0.7030 ± 0.005 and 0.7100 ± 0.005, respectively (Fig. 7 and Table S5). In the Grizzas samples, using an initial $^{87}Sr/^{86}Sr$ of 0.7100 generates model ages that are generally within uncertainty of those where the initial $^{87}Sr/^{86}Sr$ was assumed to be 0.7080; conversely, the ages are $\geq 10\,\%$ older if an initial $^{87}Sr/^{86}Sr$ value of 0.7030 is employed. Figure 7 shows that the older the sample, the more dramatic the impact of the initial $^{87}Sr/^{86}Sr$ chosen. For the > 40 Ma Grizzas micas, the use of initial $^{87}Sr/^{86}Sr$ of 0.7100 provides ages that are resolvable (i.e., outside 2 SE) from those obtained employing 0.7030 as the initial $^{87}Sr/^{86}Sr$ ratio. Conversely, for the younger (< 30 Ma) Megas Gialos samples, all the calculated model ages are within uncertainty of each other. While the favored approach remains to analyze a low Rb/Sr phase cogenetic to mica (e.g., epidote, plagioclase, carbonate, apatite) where there is limited independent knowledge of initial Sr isotope compositions, we recommend employing $^{87}Sr/^{86}Sr$ samples that are intermediate between those of likely endmembers representative of the examined lithologies.

At Grizzas, the blueschist blocks (samples SYGR36 and SYGR44) and a metasomatic rind (sample SYGR38) consistently yielded initial $^{87}Sr/^{86}Sr$ values close to 0.708, although the latter shows scattering between 0.704 and 0.710 (Fig. 3). In the literature, highly radiogenic values in metamafic and metasomatic rocks are common in the Kampos Belt, including for some metasedimentary rocks (Fig. 3). On the other hand, a metagabbro (sample SYGR50) yielded an initial $^{87}Sr/^{86}Sr$ value close to 0.705 Similarly, the metamafic greenschist (SYMG07) and veins (SYMG02 and SYMG08.3), along with additional vein and greenschist samples analyzed for bulk rock $^{87}Sr/^{86}Sr$ only from Megas Gialos, consistently yielded in situ epidote and age-corrected TIMS whole rock $^{87}Sr/^{86}Sr$ values of ~ 0.705 (Fig. 3 and Table S4). We interpret the least radiogenic values to represent the oceanic magmatic protolith (e.g., Taylor and Lasaga, 1999) and veins that have equilibrated with or sourced from metamafic rocks. In contrast, the more radiogenic signature could have been introduced by pre-subduction seafloor alteration (Voigt et al., 2018) or metasomatism by highly radiogenic fluids for the example derived from dehydration of metasedimentary rocks (Halama et al., 2011). The latter hypothesis is more consistent with the spatial association between metasedimentary and metasomatic rocks within the Grizzas shear zone. Our results demonstrate that for high-pressure metamafic rocks in subduction zones, the commonly assumed MORB-like $^{87}Sr/^{86}Sr$ value of 0.703 (Rösel and Zack, 2022) might not necessarily be representative of the initial Sr isotope composition.

6.2 Application to Syros

To further validate our newly acquired mica Rb–Sr ages (anchored to epidote or, when not available, to a modeled initial $^{87}Sr/^{86}Sr$; Table 2), we compare them with published age constraints from Kampos Belt (Top CBU) and Middle CBU localities (Fig. 8). Kotowski et al. (2022) and Glodny and Ring (2022) compiled and reported new ID TIMS Rb–Sr ages, mostly from the western Kampos Belt and outcrops along the Top CBU on Syros, ranging from 53 to 43 Ma. This age range is interpreted to date the eclogite to blueschist-facies subduction fabrics, developed during the prograde to peak pressure and earliest stage of exhumation. Robust U–Pb zircon and Lu–Hf garnet ages between 53 and 48 Ma constrain the peak metamorphism in the Grizzas area (see Tomascheck et al., 2003; Lagos et al., 2007) and are in agreement with the higher end of the Rb–Sr multi-mineral isochron ages, including white mica separates (e.g., Glodny and Ring, 2022). Recent in situ Rb–Sr dating of white mica also showed an age of 48.4 ± 3.6 Ma for an eclogite from the Katergaki cape (presumably belonging to the Top CBU), which was also interpreted to date the near-peak metamorphism (Barnes et al., 2024). At Grizzas, a blueschist block (SYGR36), an altered metagabbro (SYGR42), and a metasediment (SYGR45) yielded mica Rb–Sr ages varying from 46.6 ± 4.6 to 47.2 ± 3.8 Ma (Table 2 and Fig. 6). Similarly, the dilational vein sample SYGR41 returned a mica Rb–Sr age consistent with the HP metamorphic stage (44.7 ± 4.5 Ma). These ages overlap with the low end of the HP eclogite to blueschist-facies near-peak metamorphism (peak to the earliest exhumation). Thus, and in line with previous investigations, the obtained ages are interpreted to date near-peak metamorphism (for the blueschist SYGR36 and metasediment SYGR45 samples) and the oldest record of near-peak fluid–rock interactions and shear zone

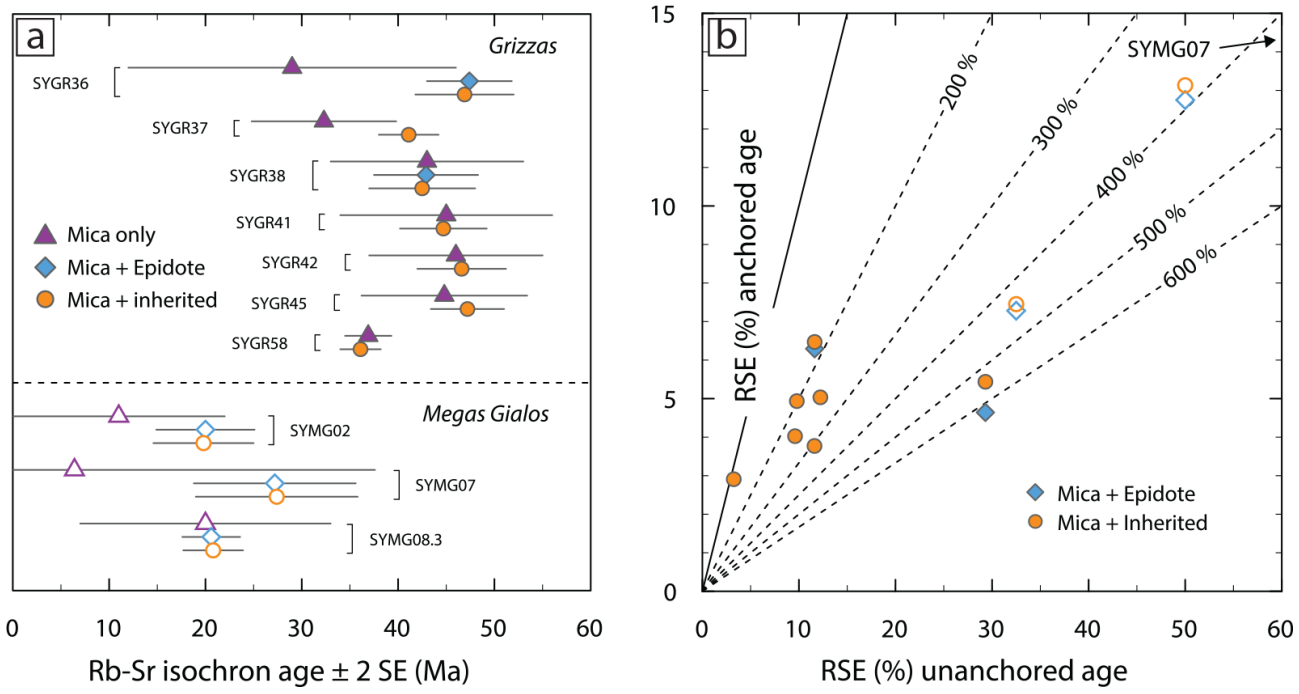

Figure 6. **(a)** Overview of mica Rb–Sr ages using mica data points only (unanchored isochrons, purple), anchoring to epidote (blue), and anchoring to an assumed initial $^{87}Sr/^{86}Sr$ composition (orange). Initial $^{87}Sr/^{86}Sr$ was assumed to be 0.7080 ± 0.0005 (2 SE) for Grizzas and 0.7050 ± 0.0005 (2 SE) for Megas Gialos (see text). **(b)** Comparison of the uncertainties expressed as percentage RSE (relative standard error) for unanchored mica-only ages and ages anchored to either epidote or an assumed initial $^{87}Sr/^{86}Sr$. Samples from Grizzas and Megas Gialos are shown as empty and full symbols, respectively. The location of the Megas Gialos sample SYMG07 (unanchored age 6.4 ± 31 Ma, 243 % RSE) is shown with an arrow.

development leading to veining (SYGR41) and metagabbro fluid-assisted deformation (SYGR42).

Kotowski et al. (2022) and Glodny and Ring (2022) noted that ages for the retrograde stage associated with early decompression in the epidote blueschist-facies are in the 45 to 40 Ma range, which could also be related to a mixed signal due to partial re-equilibration between the early lawsonite blueschist and HP greenschist-facies metamorphism. Blueschist to (HP) greenschist-facies retrogression during exhumation is constrained to occur between 40 and 20 Ma in the Kampos Belt based on previous Rb–Sr and Ar–Ar geochronology (Glodny and Ring, 2022; Kotowski et al., 2022; Laurent et al., 2017). The metasomatic rind samples SYGR37 and SYGR38 yielded mica Rb–Sr ages more consistent with metasomatism and fluid–rock interactions during the early exhumation stage in the epidote blueschist-facies stability field (41.1 ± 3.1 and 43.0 ± 5.4 Ma), although sample SYGR38 could be similarly interpreted to date the metasomatism at near-peak pressure conditions considering the age uncertainty. These ca. 43 and 41 Ma ages date continuous fluid–rock interaction during HP deformation, which preferentially occurs along shear zones (Zack and John, 2007; Angiboust et al., 2014; Kleine et al., 2014; Smit and Pogge von Strandmann, 2020; Rajič et al., 2024). Only one sample (felsic pod SYGR58) shows a statistically younger age of 36.1 ± 2.1 Ma, which is within the period of exhumation and transition from blueschist to HP greenschist-facies. This age is consistent with petrographic evidence of chlorite pseudomorphs after garnet, which is suggestive of selective greenschist-facies retrogression.

Overall, our near-peak ages align with two ages (samples 9C and 27; see Fig. 8) reported by Gyomlai et al. (2023b) for metasomatic lithologies within the Kampos Belt (Lia side), while our HP early exhumation ages are comparable, within uncertainty, to one of their ages (sample 9A). Additionally, Gyomlai et al. (2023b) obtained three ages of ca. 36 Ma (samples Ln57, Ln10, and Ln1), overlapping with our sample SYGR58 (felsic pod), which they interpreted as retrograde ages dating the "main" metasomatic event along Kampos. Our data points to at least one event of HP metasomatism and fluid–rock interactions along the Grizzas shear zone within the range of 46.6 ± 4.6 to 41.1 ± 3.1 Ma. Due to method uncertainties, distinguishing between multiple events within this time range is not feasible. Thus, our data suggest that fluid–rock interactions and metasomatism began under near-peak metamorphic conditions and continued during the early stages of HP exhumation. These results agree with Ar–Ar ages constraining the activity of the Lia shear zone (northern boundary of the Kampos Belt; see Fig. 1a) at near peak to blueschist-facies exhumation conditions in the ~ 51 to 35 Ma

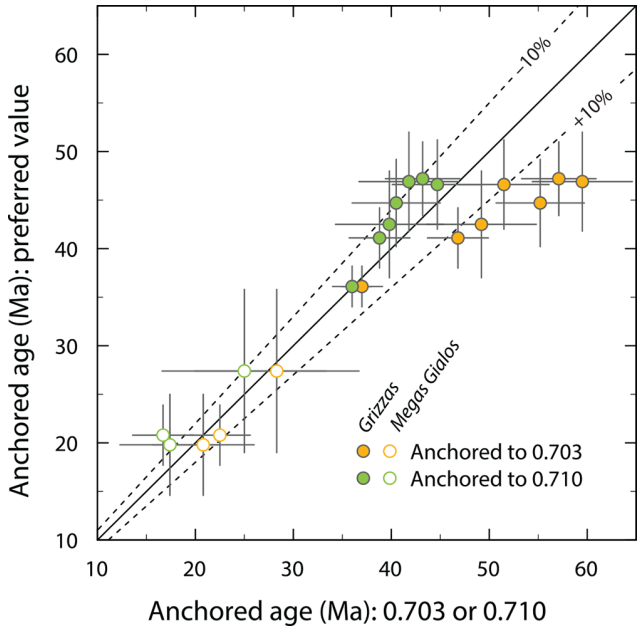

Figure 7. Covariation plots showing the effect of assumed initial $^{87}Sr/^{86}Sr$ on the mica Rb–Sr "model" age. Preferred anchoring values are 0.7080 ± 0.0005 for Grizzas and 0.7050 ± 0.0005 for Megas Gialos (vertical axis), which are compared to the extreme values in the range of observed bulk rock data for the Kampos Belt: 0.7030 ± 0.0005 (orange) and 0.7100 ± 0.0005 (green) (horizontal axis).

range (and locally down to 23 Ma due to later greenschist-facies activity; Laurent et al., 2021). Furthermore, Barnes et al. (2024) reported an in situ white mica Rb–Sr age of 44.5 ± 3.1 Ma for a metasomatic eclogite (Delfini locality; presumably Middle CUB), suggesting that metasomatism in this section of the nappe stack also initiated at HP conditions.

This enables us to constrain localized shear zone activity under HP conditions within the subduction channel in the presence of fluids. Although previous studies have attempted to estimate the P-T conditions of formation of these metasomatic lithologies along the Kampos Belt, the results vary widely, potentially suggesting that metasomatism may have occurred throughout the prograde to exhumation path (Marschall et al., 2006; Miller et al., 2009; Gyomlai et al., 2021). This is confirmed by novel reaction path thermodynamic modeling approaches, demonstrating that bulk rock compositions, particularly the activity of elements such as Ca and Mg, play a primary role in the formation of these metasomatic rocks (Codillo et al., 2022). These metasomatic and fluid–rock interaction events may thus be temporally and spatially associated with processes such as deep slicing, underplating, and slow slip and tremor (Angiboust et al., 2012; Behr et al. 2018; Agard et al., 2018; Muñoz-Montecinos et al., 2020; Tewksbury-Christle et al., 2021; Behr and Bürgmann, 2021).

In the Megas Gialos locality, the host greenschist sample yielded an age of 27.4 ± 8.4 Ma, in line with previous investigations of lithologies from the Middle CBU, which have shown ages of greenschist-facies metamorphism younger than ca. 35 Ma using Ar–Ar and ID TIMS Rb–Sr geochronology (Glodny and Ring, 2022; Bröcker et al., 2013). The vein samples SYMG02 and SYMG08.3 yielded potentially younger (although not statistically resolvable) ages of 19.8 ± 5.2 and 20.8 ± 3.1 Ma, interpreted to date dilational veining during the latest stages of exhumation of the metamorphic nappe at the base of the forearc (Cisneros et al., 2021; Muñoz-Montecinos and Behr, 2023). These ages align with phengite + glaucophane veins from the Top CBU unit (Evia), which yielded virtually identical in situ white mica Rb–Sr (anchored to glaucophane) ages for dilational veining at conditions of ca. 350 °C and 0.8 GP (Ducharme et al., 2024). Thus, the finding of similar ages for transitional blueschist to greenschist-facies dilational veining on Syros and Evia demonstrates that across-dip fluid flow toward the forearc was an ubiquitous process that occurred along the Hellenic subduction zone at ca. 20–22 Ma.

7 Summary

We systematically evaluated the limitations of mica Rb–Sr dating by LA-ICP-MS/MS for young metamafic samples using metamorphic rocks from Syros and attempted to circumvent these limitations by anchoring the initial $^{87}Sr/^{86}Sr$ component to either a low $^{87}Rb/^{86}Sr$ phase (i.e., epidote) or a modeled value. White mica analysis yielded narrow $^{87}Rb/^{86}Sr$ spread (ranging from 14 to 231 across the whole dataset), along with non-radiogenic and imprecise $^{87}Sr/^{86}Sr$ (generally < 0.8; 2 SE typically exceeding 1 %). The combined effect of low $^{87}Rb/^{86}Sr$ values, limited spread in Rb/Sr, and high uncertainty in $^{87}Sr/^{86}Sr$ resulted in mica-only ages (i.e., without anchoring) with very large uncertainties of 10 % to 35 % RSE or higher in some cases.

By anchoring these data to a low Rb/Sr phase such as epidote, age precision improved by up to 6 times, aligning with previous Rb–Sr TIMS data from Syros and other localities along the Cyclades blueschists unit. Such improvement is contingent on the employment of a MC-ICP-MS instrument to obtain accurate and precise Sr isotope values for the low Rb/Sr phase by laser ablation compared to the considerably lower precision of similar analyses by LA-ICP-MS/MS (Barnes et al., 2024). A first set of samples yielded ages consistent with near peak to early exhumation along the epidote blueschist-facies. The youngest ages likely date the latest stage of (HP) greenschist-facies exhumation. These ages are interpreted as dating various metasomatic stages that likely initiated at near-peak metamorphic conditions and continued during exhumation. We noted unexpectedly high radiogenic $^{87}Sr/^{86}Sr$ values and sometimes variability for the metamafic–metasomatic materials. These values, likely re-

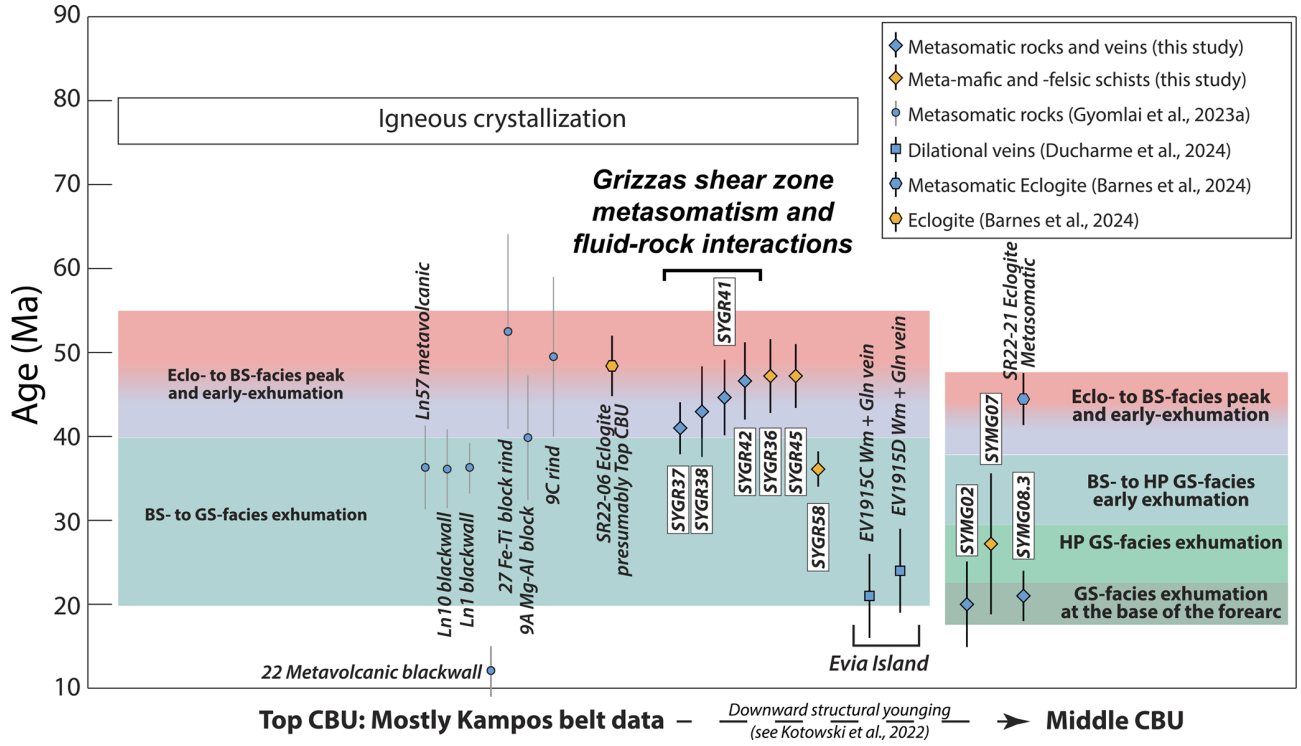

Figure 8. Summary of in situ mica Rb–Sr ages from this study and previous investigations on Syros and other localities along the CBU (Evia). The fields depicting the timing of the main tectonometamorphic events represent a synthesis of the compilations from Kotowski et al. (2022) and Glodny and Ring (2022), including white mica Rb–Sr and Ar–Ar, U–Pb in zircon, and Lu–Hf in garnet, to which the reader is referred to for a more complete compilation of the geochronological data collected on Syros and all along the CBU. BS is blueschist, Eclo is eclogite, GS is greenschist, and HP is high pressure.

sulting from focused fluid flow and metasomatism along the studied shear zone, underscore the importance of carefully selecting and evaluating the geologic context of $^{87}Sr/^{86}Sr$ anchors for future applications of this "model" Rb–Sr white mica dating methodology.

Data availability. All laser-ablation ICP-MS/MS and MC-ICP-MS data are available in the Supplement.

Supplement. The supplement related to this article is available online at: https://doi.org/10.5194/gchron-6-585-2024-supplement.

Author contributions. JMM, AG, and SV designed the study and performed the experiments with contributions from BP. JMM and WB collected the studied samples. AG and SO developed the statistical analysis. JMM and AG prepared the manuscript with contributions from all co-authors.

Competing interests. The contact author has declared that none of the authors has any competing interests.

Disclaimer. Publisher's note: Copernicus Publications remains neutral with regard to jurisdictional claims made in the text, published maps, institutional affiliations, or any other geographical representation in this paper. While Copernicus Publications makes every effort to include appropriate place names, the final responsibility lies with the authors.

Acknowledgements. We would like to thank Madalina Jaggi and Marcel Guillong for providing invaluable technical support and Heather Stoll for granting access to the Agilent 8800 employed in this work. We acknowledge the constructive reviews provided by Thomas Gyomlai and Bruno Vieira Ribeiro and acknowledge Daniela Rubatto for the editorial handling of this paper. This project was supported by the Swiss National Foundation (Ambizione fellowship no. PZ00P2_180126/1 to Andrea Giuliani) and an ERC Starting Grant (grant no. 947659) awarded to Whitney Behr.

Financial support. This research has been supported by the European Research Council through Horizon Europe (grant no. 947659) and the Schweizerischer Nationalfonds zur Förderung der Wissenschaftlichen Forschung (nccr – on the move, grant no. PZ00P2_180126/1).

Review statement. This paper was edited by Daniela Rubatto and reviewed by Thomas Gyomlai and Bruno Vieira Ribeiro.

References

Agard, P., Plunder, A., Angiboust, S., Bonnet, G., and Ruh, J.: The subduction plate interface: Rock record and mechanical coupling (from long to short timescales), Lithos, 320, 537–566, 2018.

Angiboust, S. and Glodny, J.: Exhumation of eclogitic ophiolitic nappes in the W. Alps: New age data and implications for crustal wedge dynamics, Lithos, 356, 105374, https://doi.org/10.1016/j.lithos.2020.105374, 2020.

Angiboust, S., Wolf, S., Burov, E., Agard, P., and Yamato, P.: Effect of fluid circulation on subduction interface tectonic processes: Insights from thermo-mechanical numerical modelling, Earth Planet. Sc. Lett., 357, 238–248, 2012.

Angiboust, S., Pettke, T., De Hoog, J. C., Caron, B., and Oncken, O.: Channelized fluid flow and eclogite-facies metasomatism along the subduction shear zone, J. Petrol., 55, 883–916, 2014.

Angiboust, S., Cambeses, A., Hyppolito, T., Glodny, J., Monié, P., Calderón, M., and Juliani, C.: A 100-my-long window onto mass-flow processes in the Patagonian Mesozoic subduction zone (Diego de Almagro Island, Chile), Bulletin, 130, 1439–1456, 2018.

Barnes, C. J., Zack, T., Bukała, M., Rösel, D., Mark, C., and Schneider, D. A.: Dating metamorphic processes and identifying 87Sr/86Sr inheritance using volume-coupled Rb/Sr geochronology and geochemistry of in situ white mica: A demonstration with HP/LT rocks from Syros, Greece, Chem. Geol., 660, 122149, 2024.

Bastias, J., Spikings, R., Riley, T., Chew, D., Grunow, A., Ulianov, A., Chiaradia, M., and Burton-Johnson, A.: Cretaceous magmatism in the Antarctic Peninsula and its tectonic implications, J. Geol. Soc., 180, jgs2022-067, https://doi.org/10.1144/jgs2022-067, 2023.

Behr, W. M. and Bürgmann, R.: What's down there? The structures, materials and environment of deep-seated slow slip and tremor, Philos. T. Roy. Soc. A, 379, 20200218, https://doi.org/10.1098/rsta.2020.0218, 2021.

Behr, W. M., Kotowski, A. J., and Ashley, K. T.: Dehydration-induced rheological heterogeneity and the deep tremor source in warm subduction zones, Geology, 46, 475–478, 2018.

Beinlich, A., John, T., Vrijmoed, J. C., Tominaga, M., Magna, T., and Podladchikov, Y. Y.: Instantaneous rock transformations in the deep crust driven by reactive fluid flow, Nat. Geosci., 13, 307–311, https://doi.org/10.1038/s41561-020-0554-9, 2020.

Breeding, C. M., Ague, J. J., and Bröcker, M.: Fluid–metasedimentary rock interactions in subduction-zone mélange: implications for the chemical composition of arc magmas, Geology, 32, 1041–1044, 2004.

Bröcker, M. and Enders, M.: Unusual bulk-rock compositions in eclogite-facies rocks from Syros and Tinos (Cyclades, Greece): implications for U–Pb zircon geochronology, Chem. Geol., 175, 581–603, 2001.

Bröcker, M., Baldwin, S., and Arkudas, R.: The geological significance of $^{40}Ar/^{39}Ar$ and Rb–Sr white mica ages from Syros and Sifnos, Greece: a record of continuous (re) crystallization during exhumation?, J. Metamorp. Geol., 31, 629–646, 2013.

Burg, J. P. and Bouilhol, P.: Timeline of the South Tibet–Himalayan belt: The geochronological record of subduction, collision, and underthrusting from zircon and monazite U–Pb ages, Can. J. Earth Sci., 56, 1318–1332, 2019.

Ceccato, A., Behr, W. M., Zappone, A. S., Tavazzani, L., and Giuliani, A.: Structural evolution, exhumation rates, and rheology of the European crust during Alpine collision: Constraints from the Rotondo granite – Gotthard nappe, Tectonics, 43, e2023TC008219, https://doi.org/10.1029/2023TC008219, 2024.

Cisneros, M., Barnes, J. D., Behr, W. M., Kotowski, A. J., Stockli, D. F., and Soukis, K.: Insights from elastic thermobarometry into exhumation of high-pressure metamorphic rocks from Syros, Greece, Solid Earth, 12, 1335–1355, https://doi.org/10.5194/se-12-1335-2021, 2021.

Codillo, E. A., Klein, F., Dragovic, B., Marschall, H. R., Baxter, E., Scambelluri, M., and Schwarzenbach, E.: Fluid-Mediated Mass Transfer Between Mafic and Ultramafic Rocks in Subduction Zones, Geochem. Geophys. Geosyst., 23, e2021GC010206, https://doi.org/10.1029/2021GC010206, 2022.

Cooperdock, E. H., Raia, N. H., Barnes, J. D., Stockli, D. F., and Schwarzenbach, E. M.: Tectonic origin of serpentinites on Syros, Greece: Geochemical signatures of abyssal origin preserved in a HP/LT subduction complex, Lithos, 296, 352–364, 2018.

Dalton, H., Giuliani, A., Phillips, D., Hergt, J., Maas, R., Matchan, E., Woodhead, J., and O'Brien, H.: comparison of geochronological methods commonly applied to kimberlites and related rocks: Three case studies from Finland, Chem. Geol., 558, 119899, https://doi.org/10.1016/j.chemgeo.2020.119899, 2020.

Ducharme, T. A., Schneider, D. A., Grasemann, B., Bukała, M., Camacho, A., Larson, K. P., and Soukis, K.: Syn-exhumation metasomatic glaucophane-phengite-quartz veins formed at moderate pressures: exploring the control of fO2 and bulk composition on nominally HP metamorphic assemblages, Contrib. Mineral. Petrol., 179, 1–25, 2024.

Engi, M.: Petrochronology based on REE-minerals: monazite, allanite, xenotime, apatite, Rev. Mineral. Geochem., 83, 365–418, 2017.

Fitzpayne, A., Giuliani, A., Hergt, J., Woodhead, J. D., and Maas, R.: Isotopic analyses of clinopyroxenes demonstrate the effects of kimberlite melt metasomatism upon the lithospheric mantle, Lithos, 370, 105595, https://doi.org/10.1016/j.lithos.2020.105595, 2020.

Fitzpayne, A., Giuliani, A., Howarth, G. H., Peters, B. J., Fehr, M. A., and Maas, R.: Major-, trace-element and Sr-Nd-Hf isotope geochemistry of diamondiferous dykes from Tonguma and Koidu, Sierra Leone: highly micaceous kimberlites formed by assimilation of metasomatised lithospheric mantle rocks, Chem. Geol., 630, 121475, https://doi.org/10.1016/j.chemgeo.2023.121475, 2023.

Gautier, P. and Brun, J. P.: Ductile crust exhumation and extensional detachments in the central Aegean (Cyclades and Evvia Islands), Geodinam. Acta, 7, 57–85, 1994.

Giuliani, A., Oesch, S., Guillong, M., and Howarth, G. H.: Mica RbSr dating by laser ablation ICP-MS/MS using an isochronous calibration material and application to West African kimberlites, Chem. Geol., 649, 121982, https://doi.org/10.1016/j.chemgeo.2024.121982, 2024.

Glodny, J. and Ring, U.: The Cycladic Blueschist Unit of the Hellenic subduction orogen: Protracted high-pressure

metamorphism, decompression and reimbrication of a diachronous nappe stack, Earth-Sci. Rev., 224, 103883, https://doi.org/10.1016/j.earscirev.2021.103883, 2022.

Glodny, J., Grauert, B., Fiala, J., Vejnar, Z., and Krohe, A.: Metapegmatites in the western Bohemian massif: ages of crystallisation and metamorphic overprint, as constrained by U–Pb zircon, monazite, garnet, columbite and Rb–Sr muscovite data, Geologische Rundschau, 87, 124–134, 1998.

Glodny, J., Pease, V., Montero, P., Austrheim, H., and Rusin, A. I.: Protolith ages of eclogites, Marun-Keu Complex, Polar Urals, Russia: implications for the pre-and early Uralian evolution of the northeastern European continental margin. Geological Society, London, Memoirs, 30, 87–105, 2004.

Glodny, J., Kühn, A., and Austrheim, H.: Geochronology of fluid-induced eclogite and amphibolite facies metamorphic reactions in a subduction–collision system, Bergen Arcs, Norway, Contrib. Mineral. Petrol., 156, 27–48, 2008.

Gou, L. L., Long, X. P., Yan, H. Y., Shu, T. C., Wang, J. Y., Xu, X. F., Zhou, F., and Tian, Z. B.: Metamorphic P–T Evolution and In Situ Biotite Rb–Sr Geochronology of Garnet–Staurolite Schist From the Ramba Gneiss Dome in the Northern Himalaya, Front. Earth Sci., 10, 887154, https://doi.org/10.3389/feart.2022.887154, 2022.

Gyomlai, T., Agard, P., Marschall, H. R., Jolivet, L., and Gerdes, A.: Metasomatism and deformation of block-in-matrix structures in Syros: The role of inheritance and fluid-rock interactions along the subduction interface, Lithos, 386, 105996, https://doi.org/10.1016/j.lithos.2021.105996, 2021.

Gyomlai, T., Agard, P., Jolivet, L., Larvet, T., Bonnet, G., Omrani, J.,Larson, K., Caron, B., and Noël, J.: Cimmerian metamorphism and post Mid-Cimmerian exhumation in Central Iran: Insights from in-situ Rb/Sr and U/Pb dating, J. Asian Earth Sci., 233, 105242, https://doi.org/10.1016/j.jseaes.2022.105242, 2022.

Gyomlai, T., Agard, P., Herviou, C., Jolivet, L., Monié, P., Mendes, K., and Iemmolo, A.: In situ Rb–Sr and 40Ar–39Ar dating of distinct mica generations in the exhumed subduction complex of the Western Alps, Contrib. Mineral. Petrol., 178, 58, https://doi.org/10.1007/s00410-023-02042-8, 2023a.

Gyomlai, T., Agard, P., Marschall, H. R., and Jolivet, L.: Hygrochronometry of punctuated metasomatic events during exhumation of the Cycladic blueschist unit (Syros, Greece), Terra Nova, 35, 101–112, 2023b.

Halama, R., John, T., Herms, P., Hauff, F., and Schenk, V.: A stable (Li, O) and radiogenic (Sr, Nd) isotope perspective on metasomatic processes in a subducting slab, Chem. Geol., 281, 151–166, 2011.

Halama, R., Konrad-Schmolke, M., and De Hoog, J. C.: Boron isotope record of peak metamorphic ultrahigh-pressure and retrograde fluid–rock interaction in white mica (Lago di Cignana, Western Alps), Contrib. Mineral. Petrol., 175, 20, https://doi.org/10.1007/s00410-020-1661-8, 2020.

Hogmalm, K. J., Zack, T., Karlsson, A. K. O., Sjöqvist, A. S. L., and Garbe-Schönberg, D.: In situ Rb–Sr and K–Ca dating by LA-ICP-MS/MS: an evaluation of N_2O and SF_6 as reaction gases, J. Anal. Atom. Spectrom., 32, 305–313, 2017.

Holtmann, R., Muñoz-Montecinos, J., Angiboust, S., Cambeses, A., Bonnet, G., Brown, A., Dragovic, B., Gharamohammadi, Z., Rodriguez, M., Glodny, J., Kananianm A., and Agard, P.: Cretaceous thermal evolution of the closing Neo-Tethyan realm revealed by multi-method petrochronology, Lithos, 422, 106731, https://doi.org/10.1016/j.lithos.2022.106731, 2022.

Huang, C., Wang, H., Shi, W., Sun, J., Hu, F., Xu, L., Yang, Y., Wu, S., Xie, L., and Yang, J.: In situ Rb-Sr dating of mica by LA-ICP-MS/MS, Sci. China Earth Sci., 66, 2603–2621, 2023.

Hyppolito, T., Angiboust, S., Juliani, C., Glodny, J., Garcia-Casco, A., Calderón, M., and Chopin, C.: Eclogite-, amphibolite-and blueschist-facies rocks from Diego de Almagro Island (Patagonia): Episodic accretion and thermal evolution of the Chilean subduction interface during the Cretaceous, Lithos, 264, 422–440, 2016.

Jäger, E., Niggli, E., and Wenk, E.: Rb-Sr Altersbestimmungen an Glimmern der Zentralalpen. In: Beiträge zur Geologischen Karte der Schweiz, vol. 134, Kümmerly and Frey, Bern, 1967.

John, T., Gussone, N., Podladchikov, Y. Y., Bebout, G. E., Dohmen, R., Halama, R., Klemd, R., Magna, T., and Seitz, H. M.: Volcanic arcs fed by rapid pulsed fluid flow through subducting slabs, Nat. Geosci., 5, 489–492, 2012.

Jolivet, L., Lecomte, E., Huet, B., Denèle, Y., Lacombe, O., Labrousse, L., Le Pourhiet, L., and Mehl, C.: The north cycladic detachment system, Earth Planet. Sc. Lett., 289, 87–104, 2010.

Keay, S.: The Geological Evolution of the Cyclades, Greece: Constraints from SHRIMP U-Pb Geochronology, unpublished PhD Thesis, Australian National University, Canberra, 1998.

Keiter, M., Ballhaus, C., and Tomaschek, F.: A new geological map of the Island of Syros (Aegean Sea, Greece): Implications for lithostratigraphy and structural history of the Cycladic Blueschist Unit, vol. 481, Geological Society of America, 2011.

Kirchner, K. L., Behr, W. M., Loewy, S., and Stockli, D. F.: Early Miocene subduction in the western Mediterranean: Constraints from Rb-Sr multimineral isochron geochronology, Geochem. Geophys. Geosyst., 17, 1842–1860, 2016.

Kirkland, C. L., Olierook, H. K., Danišík, M., Liebmann, J., Hollis, J., Ribeiro, B. V., and Rankenburg, K.: Dating mylonitic overprinting of ancient rocks, Commun. Earth Environ., 4, 47, https://doi.org/10.1038/s43247-023-00709-5, 2023.

Kleine, B. I., Skelton, A. D., Huet, B., and Pitcairn, I. K.: Preservation of blueschist-facies minerals along a shear zone by coupled metasomatism and fast-flowing CO_2-bearing fluids, J. Petrol., 55, 1905–1939, 2014.

Kotowski, A. J., Cisneros, M., Behr, W. M., Stockli, D. F., Soukis, K., Barnes, J. D., and Ortega-Arroyo, D.: Subduction, underplating, and return flow recorded in the Cycladic Blueschist Unit exposed on Syros, Greece, Tectonics, 41, e2020TC006528, https://doi.org/10.1029/2020TC006528, 2022.

Kutzschbach, M. and Glodny, J.: LA-ICP-MS/MS-based Rb–Sr isotope mapping for geochronology, J. Anal. Atom. Spectrom., 39, 455–477, 2024.

Lagos, M., Scherer, E. E., Tomaschek, F., Münker, C., Keiter, M., Berndt, J., and Ballhaus, C.: High precision Lu–Hf geochronology of Eocene eclogite-facies rocks from Syros, Cyclades, Greece, Chem. Geol., 243, 16–35, 2007.

Laurent, V., Huet, B., Labrousse, L., Jolivet, L., Monie, P., and Augier, R.: Extraneous argon in high-pressure metamorphic rocks: Distribution, origin and transport in the Cycladic Blueschist Unit (Greece), Lithos, 272, 315–335, https://doi.org/10.1016/j.lithos.2016.12.013, 2017.

Laurent, V., Lanari, P., Naïr, I., Augier, R., Lahfid, A., and Jolivet, L.: Exhumation of eclogite and blueschist (Cyclades, Greece):

Pressure–temperature evolution determined by thermobarometry and garnet equilibrium modelling, J. Metamorph. Gology, 36, 769–798, 2018.

Laurent, V., Scaillet, S., Jolivet, L., Augier, R., and Roche, V.: 40Ar behaviour and exhumation dynamics in a subduction channel from multi-scale 40Ar/39Ar systematics in phengite, Geochim. Cosmochim. Ac., 311, 141–173, https://doi.org/10.1016/j.gca.2021.06.001, 2021.

Li, K., Li, G. Y., Du, Y. F., Han, W., Zhang, J., Chen, L. H., Zhou, J.-B., and Li, L.: Intraslab remobilization of nitrogen during early subduction facilitates deep nitrogen recycling: Insights from the blueschists in the Heilongjiang Complex in NE China, Chem. Geol., 583, 120474, https://doi.org/10.1016/j.chemgeo.2021.120474, 2021.

Marschall, H. R., Ludwig, T., Altherr, R., Kalt, A., and Tonarini, S.: Syros metasomatic tourmaline: evidence for very high-δ11B fluids in subduction zones, J. Petrol., 47, 1915–1942, 2006.

Miller, D. P., Marschall, H. R., and Schumacher, J. C.: Metasomatic formation and petrology of blueschist-facies hybrid rocks from Syros (Greece): Implications for reactions at the slab–mantle interface, Lithos, 107, 53–67, 2009.

Muñoz-Montecinos, J. and Behr, W. M.: Transient Permeability of a Deep-Seated Subduction Interface Shear Zone, Geophys. Res. Lett., 50, e2023GL104244, https://doi.org/10.1029/2023GL104244, 2023.

Muñoz-Montecinos, J., Angiboust, S., Cambeses, A., and García-Casco, A.: Multiple veining in a paleo–accretionary wedge: The metamorphic rock record of prograde dehydration and transient high pore-fluid pressures along the subduction interface (Western Series, central Chile), Geosphere, 16, 765–786, 2020.

Muñoz-Montecinos, J., Angiboust, S., and Garcia-Casco, A.: Blueschist-facies paleo-earthquakes in a serpentinite channel (Zagros suture, Iran) enlighten seismogenesis in Mariana-type subduction margins, Earth Planet. Sc. Lett., 573, 117135, https://doi.org/10.1016/j.epsl.2021.117135, 2021.

Neumann, E. R., Griffin, W. L., Pearson, N. J., and O'Reilly, S. Y.: The evolution of the upper mantle beneath the Canary Islands: information from trace elements and Sr isotope ratios in minerals in mantle xenoliths, J. Petrol., 45, 2573–2612, 2004.

Olierook, H. K. H., Rankenburg, K., Ulrich, S., Kirkland, C. L., Evans, N. J., Brown, S., McInnes, B. I. A., Prent, A., Gillespie, J., McDonald, B., and Darragh, M.: Resolving multiple geological events using in situ Rb–Sr geochronology: implications for metallogenesis at Tropicana, Western Australia, Geochronology, 2, 283–303, 2020.

Paton, C., Woodhead, J. D., Hergt, J. M., Phillips, D., and Shee, S.: Strontium isotope analysis of kimberlitic groundmass perovskite via LA-MC-ICP-MS, Geostandards Geoanal. Res., 31, 321–330, 2007.

Paton, C., Hellstrom, J., Paul, B., Woodhead, J., and Hergt, J. I.: Freeware for the visualisation and processing of mass spectrometric data, J. Anal. Atom. Spectrom., 26, 2508–2518, 2011.

Phillips, D., Zhong, D., Matchan, E. L., Maas, R., Farr, H., O'Brien, H., and Giuliani, A.: A Comparison of Geochronology Methods Applied to Kimberlites and Related Rocks from the Karelian Craton, Finland. 11th International Kimberlite Conference, Botswana, Extended Abstract, 11IKC-4880, 2017.

Pimenta Silva, M., Marxer, F., Keller, T., Giuliani, A., Ulmer, P., and Müntener, O.: Alkaline magmas in shallow arc plutonic roots: a field and experimental investigation of hydrous cumulate melting in the southern Adamello batholith, Contrib. Mineral. Petrol., 178, 64, https://doi.org/10.1007/s00410-023-02047-3, 2023.

Plank, T.: The Chemical Composition of Subducting Sediments, in: Treatise on Geochemistry, edited by: Keeling, R. F., Elsevier, Amsterdam, 607–629, 2nd edn., https://doi.org/0.1016/B978-0-08-095975-7.00319-3, 2014.

Putlitz, B., Cosca, M. A., and Schumacher, J. C.: Prograde mica $^{40}Ar/^{39}Ar$ growth ages recorded in high pressure rocks (Syros, Cyclades, Greece), Chem. Geol., 214, 79–98, 2005.

Rajič, K., Raimbourg, H., Gion, A. M., Lerouge, C., and Erdmann, S.: Tracing the Scale of Fluid Flow in Subduction Zone Forearcs: Implications from Fluid-Mobile elements, Chem. Geol., 659, 122141, https://doi.org/10.1016/j.chemgeo.2024.122141, 2024.

Redaa, A., Farkaš, J., Gilbert, S., Collins, A. S., Wade, B., Löhr, S., Zack, T., and Garbe-Schönberg, D.: Assessment of elemental fractionation and matrix effects during in situ Rb–Sr dating of phlogopite by LA-ICP-MS/MS: implications for the accuracy and precision of mineral ages, J. Anal. Atom. Spectrom., 36, 322–344, 2021.

Redaa, A., Farkaš, J., Hassan, A., Collins, A. S., Gilbert, S., and Löhr, S. C.: Constraints from in-situ Rb-Sr dating on the timing of tectono-thermal events in the Umm Farwah shear zone and associated Cu-Au mineralisation in the Southern Arabian Shield, Saudi Arabia, J. Asian Earth Sci., 224, 105037, https://doi.org/10.1016/j.jseaes.2021.105037, 2022.

Regis, D., Rubatto, D., Darling, J., Cenki-Tok, B., Zucali, M., and Engi, M.: Multiple metamorphic stages within an eclogite-facies terrane (Sesia Zone, Western Alps) revealed by Th–U–Pb petrochronology, J. Petrol., 55, 1429–1456, 2014.

Ribeiro, B. V., Finch, M. A., Cawood, P. A., Faleiros, F. M., Murphy, T. D., Simpson, A., Glorie, S., Tedeschi, M., Armit, R., and Barrote, V. R.: From microanalysis to supercontinents: insights from the Rio Apa Terrane into the Mesoproterozoic SW Amazonian Craton evolution during Rodinia assembly, J. Metamorph. Geology, 40, 631–663, 2022.

Ribeiro, B. V., Kirkland, C. L., Finch, M. A., Faleiros, F. M., Reddy, S. M., Rickard, W. D., and Michael, I. H.: Microstructures, geochemistry, and geochronology of mica fish: Review and advances, J. Struct. Geol., 175, 104947, https://doi.org/10.1016/j.jsg.2023.104947, 2023a.

Ribeiro, B. V., Kirkland, C. L., Kelsey, D. E., Reddy, S. M., Hartnady, M. I., Faleiros, F. M., Rankenburg, K., Liebmann, J., Korhonen, F. J., and Clark, C.: Time-strain evolution of shear zones from petrographically constrained Rb–Sr muscovite analysis, Earth Planet. Sc. Lett., 602, 117969, https://doi.org/10.1016/j.epsl.2022.117969, 2023b.

Rösel, D. and Zack, T.: LA-ICP-MS/MS Single-Spot Rb-Sr Dating, Geostandards Geoanalyt. Res., 46, 143–168, https://doi.org/10.1111/ggr.12414, , 2022.

Rubatto, D., Regis, D., Hermann, J., Boston, K., Engi, M., Beltrando, M., and McAlpine, S. R.: Yo-yo subduction recorded by accessory minerals in the Italian Western Alps, Nat. Geosci., 4, 338–342, 2011.

Rubatto, D., Williams, M., Markmann, T. A., Hermann, J., and Lanari, P.: Tracing fluid infiltration into oceanic crust up to ultra-high-pressure conditions, Contrib. Mineral. Petrol., 178, 79, https://doi.org/10.1007/s00410-023-02060-6, 2023.

Salters, V. J. and Stracke, A.: Composition of the depleted mantle, Geochem. Geophys. Geosyst., 5, 2004.

Sarkar, S., Giuliani, A., Dalton, H., Phillips, D., Ghosh, S., Misev, S., and Maas, R.: Derivation of Lamproites and Kimberlites from a Common Evolving Source in the Convective Mantle: the Case for Southern African 'Transitional Kimberlites', J. Petrol., 64, egad043, https://doi.org/10.1093/petrology/egad043, 2023.

Schmidt, M. W., Vielzeuf, D., and Auzanneau, E.: Melting and dissolution of subducting crust at high pressures: the key role of white mica, Earth Planet. Sc. Lett., 228, 65–84, 2004.

Seman, S., Stockli, D. F., and Soukis, K.: The provenance and internal structure of the Cycladic Blueschist Unit revealed by detrital zircon geochronology, Western Cyclades, Greece, Tectonics, 36, 1407–1429, 2017.

Smit, M. A. and Pogge von Strandmann, A. P.: Deep fluid release in warm subduction zones from a breached slab seal, Earth Planet. Sc. Lett., 534, 116046, https://doi.org/10.1016/j.epsl.2019.116046, 2020.

Soukis, K. and Stockli, D. F.: Structural and thermochronometric evidence for multi-stage exhumation of southern Syros, Cycladic islands, Greece, Tectonophysics, 595, 148–164, 2013.

Taylor, A. S. and Lasaga, A. C.: The role of basalt weathering in the Sr isotope budget of the oceans, Chem. Geol., 161, 199–214, 1999.

Tewksbury-Christle, C. M., Behr, W. M., and Helper, M. A.: Tracking deep sediment underplating in a fossil subduction margin: Implications for interface rheology and mass and volatile recycling, Geochem. Geophys. Geosyst., 22, e2020GC009463, https://doi.org/10.1029/2020GC009463, 2021.

Tillberg, M., Drake, H., Zack, T., Kooijman, E., Whitehouse, M. J., and Åström, M. E.: In situ Rb-Sr dating of slickenfibres in deep crystalline basement faults, Sci. Rep., 10, 562, https://doi.org/10.1038/s41598-019-57262-5, 2020.

Tillberg, M., Drake, H., Zack, T., Hogmalm, J., Kooijman, E., and Åström, M.: Reconstructing craton-scale tectonic events via in situ Rb-Sr geochronology of poly-phased vein mineralization, Terra Nova, 33, 502–510, 2021.

Timmermann, H., Štědrá, V., Gerdes, A., Noble, S. R., Parrish, R. R., and Dörr, W.: The problem of dating high-pressure metamorphism: a U–Pb isotope and geochemical study on eclogites and related rocks of the Mariánské Lázně Complex, Czech Republic, J. Petrol., 45, 1311–1338, 2004.

Tomaschek, F., Kennedy, A. K., Villa, I. M., Lagos, M., and Ballhaus, C.: Zircons from Syros, Cyclades, Greece – recrystallization and mobilization of zircon during high-pressure metamorphism, J. Petrol., 44, 1977–2002, 2003.

Trotet, F., Jolivet, L., and Vidal, O.: Tectono-metamorphic evolution of Syros and Sifnos islands (Cyclades, Greece), Tectonophysics, 338, 179–206, 2001.

Tual, L., Smit, M. A., Cutts, J., Kooijman, E., Kielman-Schmitt, M., Majka, J., and Foulds, I.: Rapid, paced metamorphism of blueschists (Syros, Greece) from laser-based zoned Lu-Hf garnet chronology and LA-ICPMS trace element mapping, Chem. Geol., 607, 121003, https://doi.org/10.1016/j.chemgeo.2022.121073, 2022.

Uunk, B., Brouwer, F., ter Voorde, M., and Wijbrans, J.: Understanding phengite argon closure using single grain fusion age distributions in the Cycladic Blueschist Unit on Syros, Greece, Earth Planet. Sc. Lett., 484, 192–203, 2018.

Vermeesch, P.: IsoplotR: A free and open toolbox for geochronology, Geosci. Front., 9, 1479–1493, 2018.

Villa, I. M.: Isotopic closure, Terra nova, 10, 42–47, 1998.

Villa, I. M.: Diffusion in mineral geochronometers: Present and absent, Chem. Geol., 420, 1–10, 2016.

Villa, I. M., De Bièvre, P., Holden, N. E., amd Renne, P. R.: IUPAC-IUGS recommendation on the half life of 87Rb, Geochim. Cosmochim. Ac. 164, 382–385, 2015.

Voigt, M., Pearce, C. R., Baldermann, A., and Oelkers, E. H.: Stable and radiogenic strontium isotope fractionation during hydrothermal seawater-basalt interaction, Geochim. Cosmochim. Ac., 240, 131–151, 2018.

Volante, S., Blereau, E., Guitreau, M., Tedeschi, M., van Schijndel, V., and Cutts, K.: Current applications using key mineral phases in igneous and metamorphic geology: perspectives for the future, Geol. Soc. Lond., Special Publications, 537, 57–121, 2024.

von Blanckenburg, F., Villa, I. M., Baur, H., Morteani, G., and Steiger, R. H.: Time calibration of a PT-path from the Western Tauern Window, Eastern Alps: the problem of closure temperatures, Contrib. Mineral. Petrol., 101, 1–11, 1989.

Wang, C., Alard, O., Lai, Y. J., Foley, S. F., Liu, Y., Munnikhuis, J., and Wang, Y.: Advances in in-situ Rb-Sr dating using LA-ICP-MS/MS: applications to igneous rocks of all ages and to the identification of unrecognized metamorphic events, Chem. Geol., 610, 121073, https://doi.org/10.1016/j.precamres.2022.106872, 2022.

Wawrzenitz, N., Romer, R. L., Oberhänsli, R., and Dong, S.: Dating of subduction and differential exhumation of UHP rocks from the Central Dabie Complex (E-China): constraints from microfabrics, Rb–Sr and U–Pb isotope systems, Lithos, 89, 174–201, 2006.

Whitney, D. L. and Evans, B. W.: Abbreviations for names of rock-forming minerals, Am. Mineral., 95, 185–187, 2010.

Wirth, E. A., Sahakian, V. J., Wallace, L. M., and Melnick, D.: The occurrence and hazards of great subduction zone earthquakes, Nat. Rev. Earth Environ., 3, 125–140, 2022.

Zack, T. and Hogmalm, K. J.: Laser ablation Rb/Sr dating by online chemical separation of Rb and Sr in an oxygen-filled reaction cell, Chem. Geol., 437, 120–133, 2016.

Zack, T. and John, T.: An evaluation of reactive fluid flow and trace element mobility in subducting slabs, Chem. Geol., 239, 199–216, 2007.

Zametzer, A., Kirkland, C. L., Barham, M., Hartnady, M. I., Bath, A. B., and Rankenburg, K.: Episodic alteration within a gold-bearing Archean shear zone revealed by in situ biotite Rb–Sr dating, Precambrian Res., 382, 106872, https://doi.org/10.1016/j.precamres.2022.106872, 2022.

Zhao, H., Zhao, X. M., Le Roux, P. J., Zhang, W., Wang, H., Xie, L. W., Huang, C., Wu, S.-T., Yang, J.-H., Wu, F.-Y., and Yang, Y. H.: Natural clinopyroxene reference materials for in situ Sr isotopic analysis via LA-MC-ICP-MS, Front. Chem., 8, 594316, https://doi.org/10.3389/fchem.2020.594316, 2020.